

Starspot distribution and flare events in two young low-mass stars using TESS data

RAJIB KUMBHAKAR ¹, SOUMEN MONDAL ¹, SAMRAT GHOSH ², AND DIYA RAM ¹

¹*S.N. Bose National Centre for Basic Sciences, Kolkata 700106*

²*Aryabhata Research Institute of Observational Sciences (ARIES), Nainital 263001, India*

ABSTRACT

Wide-field high-precision photometric observations such as *Transiting Exoplanet Survey Satellite* (*TESS*) allowed the investigation of the stellar magnetic activity of cool stars. M-dwarf's starspots and stellar flares are the main indicators of magnetic activity. The present study focuses on modeling light curves (LCs) to analyze the distribution and characteristics of starspots e.g., location, temperature, and spot size. The *TESS* light curves of two selected young M-dwarfs i.e. GJ 182 and 2MASS J05160212+2214528 were reconstructed using the BASSMAN software, obtaining a three-spot model for GJ 182 and two-spot model for 2MASS J05160212+2214528, describing their light curves. For GJ 182, the mean spot temperature was estimated to be approximately 3279 K, covering 5-8.5% of the stellar surface while for 2MASS J05160212+2214528 the average spot temperature was approximately 2631 K, with a mean spottedness of about 5.4%. Using the 2-min cadence LC data, we identified and analyzed 48 flare events from GJ 182, while no flares were detected in 2MASS J05160212+2214528. The estimated bolometric flare energy ranged from $10^{32} - 10^{35}$ erg, and $10^{31} - 10^{33}$ erg in the *TESS* bandpass. We derived the power-law index of -1.53 ± 0.12 and -1.86 ± 0.22 for flare frequency distribution in sectors 5 and 32 respectively in the flare energy 10^{33} to 10^{35} erg, consistent with previous studies for M-dwarfs. A positive linear correlation between flare energy and duration was found with a slope of 0.67 ± 0.02 , suggesting a similar mechanism followed by stellar superflares and solar flares. By assuming the similarities with solar flares, we also estimated the lower limit of the magnetic field strength around 12 - 232 G to produce such superflare events.

1. INTRODUCTION

Starspots are local concentrations of magnetic fields on the stellar surface just like Sunspots. Starspots are cool and dark regions and are generated due to the stellar dynamo (Davenport 2015). The starspots' formation is due to the local suppression of convective motion by the magnetic flux tubes that block or redirect the energy flow to the surface and as a result, the region appears cool and darker than the bright photosphere (see reviews, Strassmeier 2009). In this area magnetic flux tubes aligned almost vertically (Davenport 2015). Generally, M-dwarfs are magnetically active objects, exhibiting a complex and multi-scale nature of magnetic fields. This complexity arises from their fully convective nature in the case of later-type M-dwarfs (spectral type later than M4.0) or the presence of convective layers in the upper parts of their interiors for early-type M-dwarfs (Kochukhov 2021). Being magnetically active plays a vital role in generating the stellar spots in young M-dwarfs and triggers magnetic reconnection, which serves as a primary mechanism of the energy release during stellar flares (Lin et al. 2019; Bicz et al. 2022). Therefore, starspots analysis can provide some insights into the internal dynamo activity as well as the magnetic field structure of the stars (Strassmeier 2009). We can also measure precisely the stellar rotation period by photometric analysis of the light curve (Strassmeier 2009; Davenport 2015). The larger and darker stellar spots generate light curves with larger amplitude and vice-versa. Strassmeier (2009) pointed out that so far, more than 200 billion stars have been spotted stars in our galaxy and most of them are not detected using current techniques.

Stellar flares are intense, fast-occurring phenomena triggered by magnetic reconnection in stellar coronae and dramatic releases of magnetic energy in the form of electromagnetic radiation across all wavelength (Ilin & Poppenhaeger 2022; Pietras et al. 2022). The flares in low-mass M-dwarfs are analogous to solar flares and originate due to analogous magnetic reconnection events (Pettersen 1989). But flares in M-dwarfs are more energetic and frequent than the Sun-like stars because the Sun-like stars spin down quickly whereas M-dwarfs are rapid rotators for longer time (Irwin et al. 2011; Newton et al. 2016). Moreover, due to the low surface temperature of these M-type stars weak

flares are easily detectable while detecting weak flares in Sun-like stars is very challenging due to their higher surface temperature and the parameters of weak flares on M-dwarfs are very much similar to the solar flares (Pietras et al. 2023). This rapid rotation can also enhance the magnetic activity and trigger more powerful and frequent flare events in M-dwarfs (Ilin 2021). M-dwarfs often emit stronger superflares than typical solar flares with total energy $\geq 10^{34}$ erg (Tu et al. 2020). Previously, Ilin (2021) found that flares happened in the relatively higher latitude compared to the Sun for fully convective stars which indicates the magnetic field concentrates to the stellar rotational poles.

We can not spatially resolve the starspots for the distant object, so analyzing the variation of light curves can give hints about the presence of starspots on the stellar surface. However, only examining the light curve is not enough to extract information of the location of the starspots. Therefore, it is necessary to model the light curve to get the distribution of the starspots, which are the main source of the periodic modulation of the light curve. In this work, we focus on modeling the starspots in young M-dwarfs to investigate their spatial distribution and its implications for stellar activity. The starspots' size, temperature, numbers and location could be the main indicator to understand how the superflares are triggered (Namekata et al. 2019, 2021). The temporal evolution of spots can guide the temporal change of magnetic field structure on the stellar surface (Namekata et al. 2019). In the earlier studies, several researchers investigated the starspots activity and lifetime of starspots of active young stars, cool stars and RS CVn-type stars through ground-based and space-based observations (Henry et al. 1995; Messina & Guinan 2002; Maehara et al. 2021; Namekata et al. 2019). They found that the lifetimes of starspots are proportional to the starspots area for small spots domain and for the domain in larger spots lifetime decreases as spot area increases, because of differential rotation (Henry et al. 1995). Moreover, the KEPLER light curve of GJ 1243 was modeled by two starspot models where one spot is located at a higher latitude and another at the stellar equator (Davenport et al. 2015). From the TESS light curve of GJ 1243, YZ CMi and V374 Peg, Bicz et al. (2022) also performed starspot modeling using BASSMAN package and compared the results with previous analysis. Ikuta et al. (2023) conducted starspot modeling using the TESS light curves of three M-dwarfs i.e., AU Mic, YZ CMi and EV Lac using adaptive parallel tempering algorithm. There are various methods to analyze the starspots distribution. Using direct imaging observation from the Hubble Space Telescope (HST) of the Betelgeuse (α Orionis) Gilliland & Dupree (1996) found a bright spot in the Ultraviolet wavelengths. Apart from this, microlensing observations (Heyrovský & Sasselov 2000; Hendry et al. 2002), Doppler Imaging (Strassmeier 2009), Polarimetry method (Valenti et al. 1995; Johns-Krull & Valenti 1996) are also used to probe the starspots on the surfaces of stars.

The objects in this study, GJ 182, and 2MASS J05160212+221452 (hereafter, 2M0516+2214), are both young M-dwarf stars. GJ 182 is a M0.5 dwarf star (Torres et al. 2006) located at a distance of 26.7 ± 1.7 pc (Donati et al. 2008). It has a mass of $0.60M_{\odot}$, a radius of $0.87R_{\odot}$ and an effective temperature of 3866 ± 143 K (Stassun et al. 2019). Moreover, it has a large lithium abundance, suggesting it is a very young object of age around 20 Myrs, and an active star with a high surface magnetic field (Favata et al. 1998). 2M0516+2214 is also a young Taurus member with spectral type of M4.5, initially identified by Slesnick et al. (2006). More details are mentioned in the Table 1. The selection of these objects is based on the smooth variation in the TESS light curve. GJ 182 has shown a strong starspot signature as well as a flare. Unfortunately, 2M0516+2214 has no flare events but displayed a smooth and variable phase light curve, which strongly indicates the presence of starspot signatures.

In this paper, we presented the spatial distribution of starspots of two young M-dwarfs, GJ 182 and 2MASS J05160212+2214528 (object details in Table 1) for the first time and identified flare events of GJ 182 using TESS photometry. This paper is organized as follows, in Section 2, we describe the TESS observation and measuring the rotation period, flare detection method, calculation of flare energies, and starspot modeling to the light curves. The obtained results of starspot modeling are described in Section 3 and we also presented the analysis of flare. Finally, we discussed this paper in Section 4 and summarised in Section 5.

2. TESS OBSERVATIONS AND DATA ANALYSIS

In this paper, we studied the stellar activities of the selected objects (Table 1) using the time-series photometry data from TESS due to its high precision, long duration, and continuity. TESS is a space-based NASA Explorer program telescope, launched in April 2018 and it is an all-sky transit survey equipped with four 10.5 cm telescopes with a combined field of view 24×96 degrees, also known as a sector (see Ricker et al. 2015 for details). A given sector is observed approximately in 27 days with roughly a day gap. The primary mission of TESS, completed in July

Table 1. Properties of the studied objects

Parameters	Object 1	Object 2	References
TIC ID	452763353	5800708	-
Other Name	GJ 182	2MASS J05160212+2214528	-
RA (hh:mm:sec)	04 : 59 : 34.8	05 : 16 : 02.1	(Cutri et al. 2003)
Dec (deg:mm:sec)	+01 : 47 : 00.7	+22 : 14 : 52.8	(Cutri et al. 2003)
TESS Sector	5,32	43,44,45	-
TESS Cadence	120s	120s	-
SpT	M0.5	M4.5	(Donati et al. 2008; Slesnick et al. 2006)
Distance (pc)	26.7 ± 1.7	181.68	(Donati et al. 2008; Bailer-Jones et al. 2018)
Temperature (K)	3866 ± 143	3025 ± 122	(Stassun et al. 2019)
Radius (R_{\odot})	0.87	0.82	(Stassun et al. 2019; Herczeg & Hillenbrand 2014)
Mass (M_{\odot})	0.60	0.09	(Stassun et al. 2019)
Age (Myr)	25	—	(Donati et al. 2008)
$v \sin i$ (km/s)	10	15.7	(Donati et al. 2008; Kraus et al. 2017)
inclination angle (deg)	60	24.48*	(Donati et al. 2008)

NOTE—* computed using rotation period, radius and rotational velocity ($v \sin i$)

2020, covered 26 sectors in both hemispheres that cover about 85% of the sky. The next 29 sectors (from 27 to 55) are observed in the first extended part of the mission. During the primary mission, two cadences were realized: a 2-minute short cadence and a 30-minute long cadence for full-frame images (FFIs). But during the first extended part of the mission, two short-time cadences, 2-min, and 20-s for a few selected sources, while a 10-min cadence is available for FFIs with an angular resolution of 21 arcsecs per pixel. TESS covers the wavelength range from 600-1000 nm centered at 786.5 nm with slightly redder than the Kepler band. We have selected two young M-dwarfs and analyzed the TESS 2-min cadence data. TESS observed 2M0516+2214 in sectors 43, 44, and 45 while 5 and 32 sectors were used to observe the GJ 182. Using the TESS Science Processing Operations Center pipeline (SPOC; Jenkins et al. 2016), light curves are automatically generated for all 2-min cadence TESS targets and made publicly available on Mikulski Archive for Space Telescopes (MAST) ¹. The light curve data products of TESS contain both Simple Aperture Photometry (SAP) and Pre-Search Data Conditioned (PDCSAP) flux data. Here, we used the ‘lightkurve’ (Lightkurve Collaboration et al. 2018) package to download the TESS light curve from MAST. In our analysis, we used PDCSAP data as PDCSAP light curves are free from instrumental effects and long-term trends due to possible systematic effects. Also, the SPOC pipeline corrects for the dilution from other nearby stars in and around the TESS aperture, as denoted by the CROWDSAP value in the TESS header files. The values of CROWDSAP indicate how much flux is due to the object only in the selected aperture. In addition, we chose to use only the data with QUALITY= 0 as the non-zero value of QUALITY denotes the data has been compromised to some degree by instrumental effects. We also filtered the data by removing NaNs. Furthermore, we removed the outliers and normalized each light curve by dividing each flux by the target’s mean flux.

2.1. Measuring Rotation Periods in TESS

Stellar rotation is an important physical characteristic for understanding the physical properties of individual stars and their populations. Rotation drives the stellar dynamo which can give rise to stellar activity e.g. starspots, and flares (Choudhuri 2017). Such starspots also co-rotate with the stars into and out of view, producing periodicity in the light curve. If the starspots do not evolve in time, then we would get a perfect periodicity over a full rotation of stars. But starspots are not stationary; rather they change shape, appear, and then vanish over time as the star rotates

¹ <https://mast.stsci.edu/portal/Mashup/Clients/Mast/Portal.html>

Table 2. Rotation periods in days from TESS data

Object	Sector	Rotation Periods (this work)		Rotation period (previous studies)								
		Period1	Period2	Wright	Messina	Magaudda	Bustos	Vach	Donati	Vidotto	Kiraga	Byrne
GJ 182	05	4.370	4.348 ± 0.016	1.86	4.43	1.86	4.41	4.4	4.35	4.35	4.41	4.56
	32	4.400	4.384 ± 0.042									
2M0516+2214	43	1.103	1.101 ± 0.002									
	44	1.102	1.101 ± 0.001									
	45	1.102	1.101 ± 0.004									

NOTE—Period1=Periods determined using NASA EXOPLANET ARCHIVE PERIODOGRAM SERVICE. Period2= Periods computed using the Gaussian Process. Wright=Wright et al. (2011), Messina=Messina et al. (2017), Magaudda=Magaudda et al. (2020), Bustos=Ibanez Bustos et al. (2023), Vach=Vach et al. (2024), Donati=Donati et al. (2008), Vidotto=Vidotto et al. (2014). Kiraga=Kiraga & Stepień (2007), Byrne=Byrne et al. (1984).

(Namekata et al. 2019). As a result, the light curves exhibit a quasi-periodic variability rather than a fully periodic variation. This implies that it is difficult to infer rotation periods using only straightforward sinusoidal variability models which are precise up to a limit. In this work, we used two different non-inference-based methods to estimate the possible periodicity in the light curves such as Lomb-Scargle periodograms (Lomb 1976), and Gaussian process (Angus et al. 2018; Scargle 1982). Here we briefly discussed the two methods below:

(i) *Lomb-Scargle (LS) Periodogram*: The Lomb-Scargle (LS) (Lomb 1976; Scargle 1982) is a well-known algorithm in observational astronomy to detect and characterize periodic signals from unevenly sample time-series data. It uses a Fourier-like power spectrum estimator, in which the time series is decomposed into a linear combination of sinusoidal functions, and the data is transformed from the time domain to the frequency domain based on sinusoidal functions. We estimated the rotation periods using the LS method implemented by NASA Exoplanet Archive Periodogram Service²(Akeson et al. 2013). Additionally, we also looked for periods using Astropy (Astropy Collaboration et al. 2013a, 2018a) package. The power spectrums of the selected objects were shown in the middle panel in Fig 3 and Fig 4.

(ii) *Gaussian Process (GP) Regression*: We also estimated the rotation periods using the GP method as described in Angus et al. (2018). This method is slower than other approaches (e.g. LS, PDM, etc.) to infer the rotation period, but the GP method can deal with the non-sinusoidal, unevenly spaced, and more complex variation in the time-series data. It offers a probabilistic framework for rotation period estimation. In addition, it allows us to assess the posterior distribution across time and, as a result, to get useful error estimates. Furthermore, Angus et al. (2018) tested GP and found that it provides slightly more accurate rotation periods than the periodogram or autocorrelation function methods and can be applied to non-uniformly sampled time-series data. We used STARSPT³, a PYTHON module to measure the rotation period using Gaussian Process. It used fast and scalable *exoplanet* (Foreman-Mackey et al. 2021) and *celerite* (Foreman-Mackey et al. 2017a; Foreman-Mackey 2018) package to fit stellar variability and modeled the rotation periods in each TESS sectors individually. Here, PyMC3 supports a variety of general GP models. Then the systematic-corrected light curves using a RotationTerm Gaussian Process kernel. As an example, we have shown a posterior distribution of the rotation period for GJ 182, measured from TESS time-series data of sectors 5 and 32 in figure 1. The estimated rotation periods using the GP method for our selected objects are consistent with the rotation periods derived from other methods. For more details on Gaussian processes in the field of astronomy, see Foreman-Mackey et al. (2017b). The rotation periods are tabulated in Table 2 and we adopted the rotation periods estimated using the GP method.

² <https://exoplanetarchive.ipac.caltech.edu/cgi-bin/Pgram/nph-pgram>

³ <https://github.com/RuthAngus/starspot>

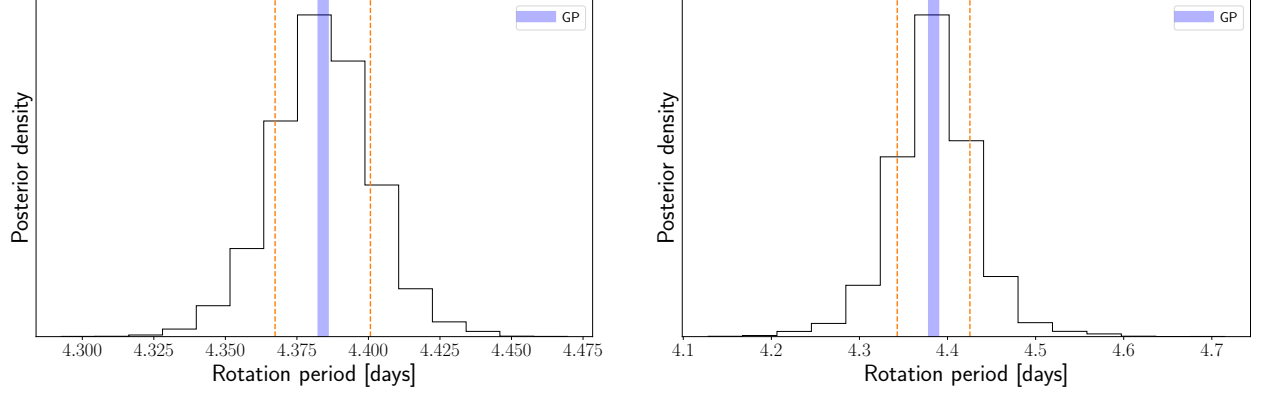


Figure 1. Posterior models of rotation periods of GJ 182, measured from TESS 2-min cadence data in sector 5 (left) and sector 32 (right) are shown here. The violet-blue line represents the rotation periods and the orange lines are the uncertainties of the periods.

2.2. Flare Detection Method

We used ALTAIPONY⁴ (Ilin 2021), an open source *python* based package to detect the flare events from the *TESS* and *Kepler* lightcurves and to estimate the flare parameters of each event. Initially, we applied a detrending approach to remove astrophysical trend-like modulation due to the starspots and instrumental trends from the time series data. To detrend the PDCSAP lightcurves, we used a custom detrending method⁵. A third-order spline function is fitted through non-gap portions of the light curve and subtracted, which removes long-term trends and starspot variability. Then, the strong sinusoidal signal is removed iteratively from the light curves. This iteration process first masks outliers points using the σ -clipping method. When the light curve showed a single outlier above 3σ , it treated the data point as a pure outlier. At the same time, there is a number of series of data points present above 3σ , it masked as a flare candidate. LS periodogram is calculated in each iteration. A cosine function fit is generated using the dominant frequency determined through a least-square procedure. The light curve was then subtracted from this cosine fit, and this procedure continued until the dominant peak's signal-to-noise ratio (SNR) decreased to 1. Finally, any non-sinusoidal variability was eliminated using two third-order Savitzky-Golay filters (Savitzky & Golay 1964) with window size 6 hours and 3 hours respectively. To detrend the light curve in sector 5 we used cubic spline with spline_coarseness value of 8 hours. Spline_coarseness is how densely the spline points are distributed in the time-series data. For sector 32 we apply the cubic spline order with spline coarseness of 6 hours. In both sectors, we used the 3σ threshold for outlier rejection as '*max_sigma*' in the custom detrending method. and such method is also described in Ilin & Poppenhaeger (2022).

To identify the flare events, we followed a similar method as described in Chang et al. (2015). ALTAIPONY uses *FlareLightCurve.find_flares()* to identify flare candidate data points. This process involved the use of three parameters, namely N1, N2, and N3, with values set to 3, 2, and 3, respectively, establishing the criteria for flare event detection. Following detrending and flare identification in ALTAIPONY, a visual inspection of all flare lightcurves was conducted to check for any inconsistency. The key characteristics considered were a distinct sharp rise and slow exponential decay. Furthermore, we again zoomed in on the particular flare region and checked visually that three consecutive data points must surpass the 3σ threshold of the light curve and be spared at least 6 minutes above it. We excluded those flare events which do not meet this criteria. The detrended light curves of GJ 182 in both sectors are shown in figure 2. In this study, we have detected 48 flare events of GJ 182 in both sectors. Most of the flares have multiple peaks in the decay phase and complex nature, further discussed in section 4.1.

2.3. Flare Energy Calculation

We have estimated the total energy of the flare by two different methods. In the first method, we determined the total flare energy of each flare using the method described in Shibayama et al. 2013; Kumbhakar et al. 2023. The total energy of the flare is calculated using stellar luminosity, amplitude, flare duration, and equivalent duration

⁴ <https://github.com/ekaterinailin/AltaiPony>

⁵ <https://altaipony.readthedocs.io/en/latest/tutorials/detrend.html>

(ED). ED is defined as the unit of time, during when a substellar object (in its quiescent state) would have emitted the same amount of energy as the flare emitted. It is measured by the area under the flare light curve (Hawley et al. 2014). The amplitude, flare duration, and ED were obtained directly from the ALTAIPONY software. According to previous work (Kumbhakar et al. 2023), the white light flare can be assumed as hot-blackbody radiation with a constant temperature of 10,000 K (denoted as T_{flare}) (Kowalski et al. 2013; Howard et al. 2018). Additionally, we used a synthetic photospheric spectrum of GJ 182 to calculate the stellar luminosity. The synthetic photospheric spectrum was generated using the BT-Settl model using the VOSA web service⁶(Allard et al. 2012). The bolometric flare luminosity is determined using T_{flare} and the area of the flare (A_{flare}) by the following equation:

$$L_{flare} = \sigma T_{flare}^4 A_{flare} \quad (1)$$

where σ is the Stefan-Boltzmann constant. The area of the flare is estimated as follows,

$$A_{flare} = (\Delta F/F) \pi R_{star}^2 \frac{\int R_{\lambda} F(\lambda, T_{eff}) d\lambda}{\int R_{\lambda} B(\lambda, T_{flare}) d\lambda} \quad (2)$$

where R_{λ} is the TESS response function, λ is the wavelength, $F(\lambda, T_{eff})$ is the flux of the synthetic photospheric spectrum of the flaring object and $B(\lambda, T_{flare})$ is the Planck function at the flare temperature. $\frac{\Delta F}{F} = \frac{F_i - F_0}{F_0}$ is referred to as the relative flare amplitude, where F_i is the stellar brightness and F_0 is the local mean flux in the quiescent state of the object. Now, the bolometric energy of the flare is obtained by integrating the bolometric flare luminosity (L_{flare}) throughout the flare duration as follows,

$$E_{flare} = \int L_{flare}(t) dt = \sigma T_{flare}^4 \times \pi R_{star}^2 \frac{\int R_{\lambda} F(\lambda, T_{eff}) d\lambda}{\int R_{\lambda} B(\lambda, T_{flare}) d\lambda} \times \int \frac{\Delta F}{F} dt \quad (3)$$

The last time-integrated factor is generally denoted as the equivalent duration of the flare in which the integration was done of relative flux within the flare duration (Hawley et al. 2014; Ikuta et al. 2023; Kumbhakar et al. 2023).

In the second method, to estimate the flare energy in the TESS bandpass, we used the modified method proposed by Kovári et al. (2007) and described in further detail in Vida et al. (2019); Pietras et al. (2022). To determine the energy of the detected flares, we integrated the normalized flare intensity during the flare event,

$$\epsilon_f = \int_{t_1}^{t_2} \left(\frac{I_{0+f}(t)}{I_0} - 1 \right) dt \quad (4)$$

where t_1 and t_2 are the begin and end times of the flare event, I_{0+f} and I_0 are the intensities with and without a flare. This integral gives the relative flare energy or equivalent duration of the flare (Vida et al. 2019) which was already calculated using ALTAIPONY. We estimated the quiescent luminosity by using the synthetic photosphere spectrum of the flared objects. The spectrum was generated with the help of the BT-Settl model grid⁷. The parameters $\log(g)$, T_{eff} , metallicities of the respective flared objects were taken from Stassun et al. (2019) to generate the theoretical spectrum. The quiescent stellar luminosity of the star was determined by multiplying the spectrum of the star $F(\lambda)$ with the TESS bandpass $R_{TESS}(\lambda)$ and the effective area of the stars with Radius R and integration was done in the interval of the wavelengths of the TESS bandpasses (λ_1, λ_2).

$$L_{star} = \pi R_{star}^2 \int_{\lambda_1}^{\lambda_2} F(\lambda) R_{TESS}(\lambda) d\lambda \quad (5)$$

Now, to calculate the flare energy in the TESS bandpass (E_f), we had to multiply the relative flare energy or ED by the quiescent stellar luminosity (L_{star}) as follows

$$E_f = L_{star} \cdot \epsilon_f = L_{star} \cdot ED \quad (6)$$

The estimated flare energy using this 2nd method was not bolometric like the method proposed by Shibayama et al. (2013). So, the energy using the 2nd method provides a lower value than the 1st method. The flare parameters and flare energies were estimated using two methods mentioned in Table 3 and 4.

⁶ <http://svo2.cab.inta-csic.es/theory/newov2/>

⁷ <http://svo2.cab.inta-csic.es/theory/newov2/>

Table 3. The estimated flare parameters of confirmed flare events from the 2-min cadence TESS data of GJ 182 from sector 5 in this work.

t_s [BTJD]	t_f [BTJD]	a	Dur	ED	E_{bol}^{syn}	E_{tess}	Magnetic Field
[Time-2457000]	[Time-2457000]	[Rel. Flux]	[min]	[Sec]	[erg]	[erg]	[G]
1438.6743	1438.7104	0.038	52.0	25.76 ± 0.18	$1.74\text{e}+34$	$8.83\text{e}+32$	79.8
1439.8744	1440.0105	0.030	196.0	120.53 ± 0.40	$8.13\text{e}+34$	$4.13\text{e}+33$	172.6
1442.6147	1442.6953	0.005	116.0	21.36 ± 0.38	$1.44\text{e}+34$	$7.32\text{e}+32$	72.7
1443.1175	1443.1217	0.003	6.0	0.87 ± 0.09	$5.90\text{e}+32$	$2.99\text{e}+31$	14.7
1444.0412	1444.0717	0.006	44.00	8.31 ± 0.31	$5.60\text{e}+33$	$2.85\text{e}+32$	45.3
1444.8078	1444.8134	0.004	8.0	1.20 ± 0.10	$8.06\text{e}+32$	$4.10\text{e}+31$	17.2
1446.1134	1446.2065	0.020	134.0	45.89 ± 0.34	$3.09\text{e}+34$	$1.57\text{e}+33$	106.5
1446.4190	1446.5634	0.124	208.0	218.63 ± 0.31	$1.47\text{e}+35$	$7.49\text{e}+33$	232.5
1447.1801	1447.2232	0.013	62.0	20.09 ± 0.25	$1.35\text{e}+34$	$6.88\text{e}+32$	70.5
1447.7787	1447.7829	0.003	6.0	0.91 ± 0.09	$6.11\text{e}+32$	$3.10\text{e}+31$	15.0
1449.3329	1449.3857	0.014	76.0	28.68 ± 0.29	$1.93\text{e}+34$	$9.83\text{e}+32$	84.2
1449.6621	1449.7024	0.013	58.0	12.17 ± 0.21	$8.20\text{e}+33$	$4.17\text{e}+32$	54.9
1449.8135	1449.8176	0.003	6.0	0.77 ± 0.09	$5.18\text{e}+32$	$2.63\text{e}+31$	13.8
1452.2204	1452.2274	0.003	10.0	1.36 ± 0.11	$9.19\text{e}+32$	$4.67\text{e}+31$	18.4
1453.2996	1453.3163	0.004	24.0	3.68 ± 0.18	$2.48\text{e}+33$	$1.26\text{e}+32$	30.2
1453.5066	1453.5135	0.002	10.0	1.10 ± 0.11	$7.38\text{e}+32$	$3.75\text{e}+31$	16.5
1453.7677	1453.7760	0.007	12.0	2.40 ± 0.11	$1.62\text{e}+33$	$8.23\text{e}+31$	24.4
1454.0607	1454.0691	0.007	12.0	2.62 ± 0.11	$1.77\text{e}+33$	$8.99\text{e}+31$	25.5
1454.2191	1454.2357	0.007	24.0	5.74 ± 0.16	$3.87\text{e}+33$	$1.96\text{e}+32$	37.7
1456.2094	1456.2371	0.007	40.0	8.76 ± 0.22	$5.90\text{e}+33$	$3.00\text{e}+32$	46.5
1457.0371	1457.0455	0.005	12.0	1.95 ± 0.12	$1.32\text{e}+33$	$6.69\text{e}+31$	22.0
1457.3913	1457.4260	0.007	50.0	9.92 ± 0.23	$6.69\text{e}+33$	$3.40\text{e}+32$	49.5
1459.7233	1459.7552	0.004	46.0	6.72 ± 0.24	$4.53\text{e}+33$	$2.30\text{e}+32$	40.8
1460.4482	1460.6121	0.090	236.0	183.44 ± 0.35	$1.24\text{e}+35$	$6.29\text{e}+33$	213.0
1462.5482	1462.5857	0.029	54.0	22.65 ± 0.19	$1.53\text{e}+34$	$7.761\text{e}+32$	74.8

NOTE— t_s : Start time of flare, t_f : Stop time of flare, a : relative amplitude of flare, Dur : duration of flare, ED : equivalent duration of flare, E_{bol}^{syn} : Bolometric energy of flare by taking the synthetic spectra of the object, E_{tess} : Flare energy in TESS bandpass.

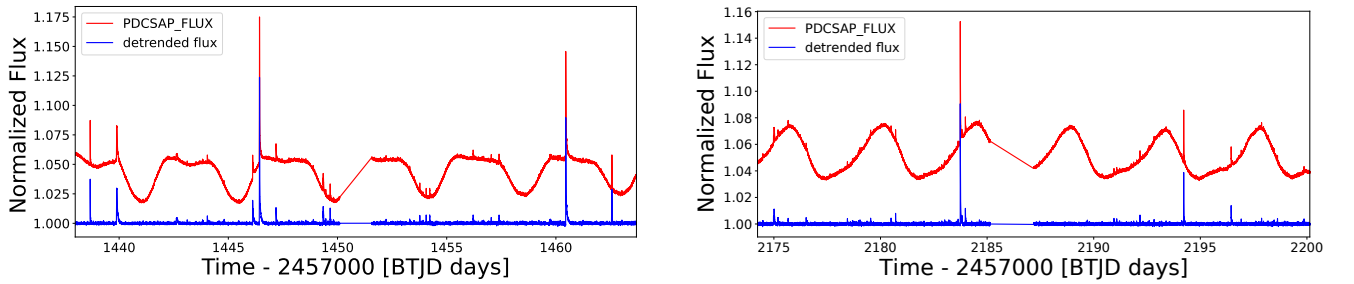


Figure 2. The PDCSAP and detrended light curves of GJ 182 for sector 5 (left) and sector 32 (right). The x-axis represents time, in Barycentric TESS Julian Days (BTJD), and the y-axis represents the normalized TESS flux. PDCSAP data are shown in red and the detrended flux data is shown in blue.

Table 4. The estimated flare parameters of confirmed flare events from the 2-min cadence TESS data of GJ 182 from sector 32 in this work.

t_s [BTJD]	t_f [BTJD]	a	Dur	ED	E_{bol}^{syn}	E_{tess}	Magnetic Field
[Time-2457000]	[Time-2457000]	[Rel. Flux]	[min]	[Sec]	[erg]	[erg]	[G]
2174.4825	2174.4908	0.003	12.0	1.41 ± 0.13	$9.51\text{e}+32$	$4.83\text{e}+31$	18.7
2174.9797	2174.9936	0.006	20.0	3.75 ± 0.15	$2.53\text{e}+33$	$1.28\text{e}+32$	30.5
2175.0005	2175.0478	0.011	68.0	25.04 ± 0.28	$1.69\text{e}+34$	$8.58\text{e}+32$	78.7
2175.1811	2175.2186	0.005	54.0	9.89 ± 0.26	$6.67\text{e}+33$	$3.39\text{e}+32$	49.4
2175.6672	2175.6742	0.004	10.0	1.68 ± 0.11	$1.13\text{e}+33$	$5.75\text{e}+31$	20.4
2176.5131	2176.5284	0.005	22.0	3.64 ± 0.16	$2.45\text{e}+33$	$1.25\text{e}+32$	30.0
2178.4423	2178.4562	0.004	20.0	3.00 ± 0.16	$2.02\text{e}+33$	$1.03\text{e}+32$	27.2
2178.6826	2178.6951	0.003	18.0	2.18 ± 0.16	$1.47\text{e}+33$	$7.46\text{e}+31$	23.2
2179.5312	2179.5437	0.004	18.0	3.46 ± 0.16	$2.33\text{e}+33$	$1.18\text{e}+32$	29.2
2180.4965	2180.5020	0.004	8.0	1.33 ± 0.10	$8.94\text{e}+32$	$4.55\text{e}+31$	18.1
2180.7062	2180.7132	0.008	10.0	2.52 ± 0.11	$1.70\text{e}+33$	$8.64\text{e}+31$	25.0
2182.9923	2182.9965	0.002	6.0	0.56 ± 0.09	$3.81\text{e}+32$	$1.93\text{e}+31$	11.8
2183.0048	2183.0243	0.003	28.0	3.13 ± 0.19	$2.11\text{e}+33$	$1.07\text{e}+32$	27.8
2183.7396	2183.8340	0.091	136.0	100.93 ± 0.26	$6.80\text{e}+34$	$3.46\text{e}+33$	158.0
2183.9743	2184.0104	0.012	52.0	14.81 ± 0.24	$9.98\text{e}+33$	$5.07\text{e}+33$	60.5
2189.7007	2189.7063	0.003	8.0	1.04 ± 0.10	$7.01\text{e}+32$	$3.56\text{e}+31$	16.0
2190.3882	2190.3924	0.002	6.0	0.66 ± 0.09	$4.46\text{e}+32$	$2.27\text{e}+31$	12.8
2190.9493	2190.9576	0.004	12.0	1.80 ± 0.12	$1.21\text{e}+33$	$6.16\text{e}+31$	21.1
2192.1715	2192.1799	0.007	12.0	2.05 ± 0.11	$1.38\text{e}+33$	$7.01\text{e}+31$	22.5
2194.1257	2194.1326	0.002	10.0	1.26 ± 0.12	$8.50\text{e}+32$	$4.32\text{e}+31$	17.7
2194.2187	2194.2590	0.039	58.0	22.53 ± 0.19	$1.52\text{e}+34$	$7.72\text{e}+32$	74.6
2196.4437	2196.4812	0.014	54.0	14.49 ± 0.22	$9.77\text{e}+33$	$4.96\text{e}+32$	59.8
2199.8631	2199.8728	0.004	14.0	1.76 ± 0.13	$1.18\text{e}+33$	$6.02\text{e}+31$	20.8

NOTE— t_s : Start time of flare, t_f : Stop time of flare, a : relative amplitude of flare, Dur : duration of flare, ED : equivalent duration of flare, E_{bol}^{syn} : Bolometric energy of flare by taking the synthetic spectra of the object, E_{tess} : Flare energy in TESS bandpass.

2.4. Estimation of Magnetic Field Strength from Flare Energy

GJ 182 is a young M-type object exhibiting significant magnetic activity. Previously, [Lang et al. \(2012\)](#) reported a large-scale average magnetic field for this object around 172 G measured from spectropolarimetric measurements, and from unpolarized spectroscopy, they provided an average magnetic field (small+large-scale field) of 2.5 kG ([Reiners & Basri 2009](#)). Interestingly, we also identified most of the flare events (35 out of 48) were in the superflare energy range, ranging from 10^{32} to 10^{34} erg which indicated it's magnetic activity nature. Therefore, by assuming the similarities between the physical process in solar flares and the flares in those VLMs and BDs and found a rough estimation of the lower limit of maximum magnetic field strength (B_m) associated with those flares by using a scaling relation that has been reported by several authors i.e. [Aulanier et al. \(2013\)](#); [Notsu et al. \(2013\)](#); [Paudel et al. \(2018\)](#). According to [Aulanier et al. \(2013\)](#), stellar flares occur when a particular fraction of magnetic energy from the star is released through an active region. The active region is assumed to be associated with positive and negative polarity (bipolar spot) with a linear separation L_{bi} and we considered the corresponding maximum magnetic field strength was B_m in the active regions on the stellar surface. In a simplified way, let's assume a portion (f) of B_m throughout the volume V_f in the atmosphere is reconnected in order to power the flare. Again, we considered the volume V_f to be equal to some fraction f' of the volume of a cube with sides of length L_{bi} . According to these assumptions, the magnetic energy released in the flare as a whole can be written as $E_f = 0.04 \times f^2 f' B_m^2 L_{bi}^3$ (see [Aulanier et al. 2013](#); [Paudel et al. 2020](#)

for more details). Furthermore, based on the model calculation performed by [Aulanier et al. \(2013\)](#) to calculate the flare energy for the Sun, they found that f and f' to be equal to 0.2. This value indicates that only about 20% of the maximum field strength was required to power the flare and only about 20% of the available volume needed to participate in the flare events. To set the lower limit of B_m , we considered the upper limit of L_{bi} and the upper limit of L_{bi} would be set if the two poles (bipolar spots) in the active regions are well separated on the stellar surface. In the limiting case, $L_{bi} = \pi \cdot R_{star}$ and the above equation is modified as follows, $E_{flare} \approx 4 \times 10^{-4} B_m^2 (\pi R_{star})^3$. Therefore, to generate the bolometric flare energies in the range 10^{32-35} erg (mentioned in Table 3 and 4), we estimated the lower limits on B_m of our objects from 15 G to 232 G. We assumed that two bi-poles are placed at both poles or 180 degrees apart on the stellar surface, the field can be considered as the global field of the objects. The lower limit of B_m derived in this work is reported in the last column of Table 3 and 4. Our estimated result is almost similar to those of [Namekata et al. \(2017\)](#); [Pietras et al. \(2022\)](#). For instance, [Namekata et al. \(2017\)](#) also found roughly the same magnetic field strength of about 30 G to 300 G for the solar-type stars using Kepler 30-min cadence data. Similarly, [Pietras et al. \(2022\)](#) reported average magnetic field strength values between 10 G to 200 G for 25,000 stars using TESS 2-minute cadence data.

2.5. Starspot Modeling

Starspots, prominent features on the surfaces of young M dwarfs, are recognized as significant contributors to periodic or quasi-periodic variations observed in the light curves of these stellar objects. Here, two selected young M dwarfs exhibited periodic variation in the phase folded light curve which might be the cause of the rotational modulation of starspots co-rotating with the objects, periodically coming into and out of view. However, the significance of these periodic variations fails to provide comprehensive insights into the properties of starspots. To qualitatively trace the sizes and position of starspots we conducted an in-depth analysis of TESS light curves utilizing the starspot modeling software, BASSMAN⁸ (Best rAndom StarSpots Model calculAtioN) ([Bicz et al. 2022](#)). In BASSMAN, the surface map of stars is considered a vector of spherical harmonic coefficients. It can be also expressed as a linear combination of spherical harmonics with an index increasing by degree l and order m . During the modeling of the light curve, the assumption of spots is spherical. The only parameter i.e. longitude of the spot varies in time due to the rotation of the stars. Here, we have recorded the longitudes of spots at phase=0. The code employed the Markov Chain Monte Carlo (MCMC) method to recreate the light curve of the spotted stars. As a result, the output provides amplitudes, sizes, latitudes, and longitudes of starspots. Here, the software approximates the “starspots” as the whole active regions that consist of several individual spots. They are not the same as the sunspot structure. To better understand the spot evolution it is necessary to divide the light curves into time segments so that each segment contains the full rotation of the object and model each modulation separately. This method is helpful to reveal changes in spot configuration from modulation to modulation. For the goodness of fit of individual models, we check the value of log probability. The higher value of log-probability indicated the better fit of the light curves and finally compared the model estimated parameters with the analytical solution. Actually, BASSMAN provides the values of mean spot temperature and percentage spottedness of the star and also calculates these parameters from the analytic solution, taken from [Notsu et al. \(2019\)](#). The analytic relations of mean spot temperature,

$$T_{spot} = 0.751T_{star} - 3.58 \times 10^{-5}T_{star}^2 + 808 \quad (7)$$

and the spot area can be estimated as follows,

$$A_{spot} = \frac{\Delta F}{F} A_{star} \left[1 - \left(\frac{T_{spot}}{T_{star}} \right)^4 \right]^{-1} \quad (8)$$

where T_{star} =effective temperature of the object, T_{spot} =the mean temperature of starspot, $\frac{A_{spot}}{A_{star}}$ is the percentage of spottedness of the object, $\frac{\Delta F}{F}$ is the normalized amplitude of light curve variations.

3. RESULTS

TESS observed GJ 182 in sectors 5 and 32 while 2M0512+2214 was observed in sectors 43, 44, and 45. We estimated the rotation period using the LS periodogram and Gaussian process. Both methods almost calculated the

⁸ <https://github.com/KBicz/BASSMAN>

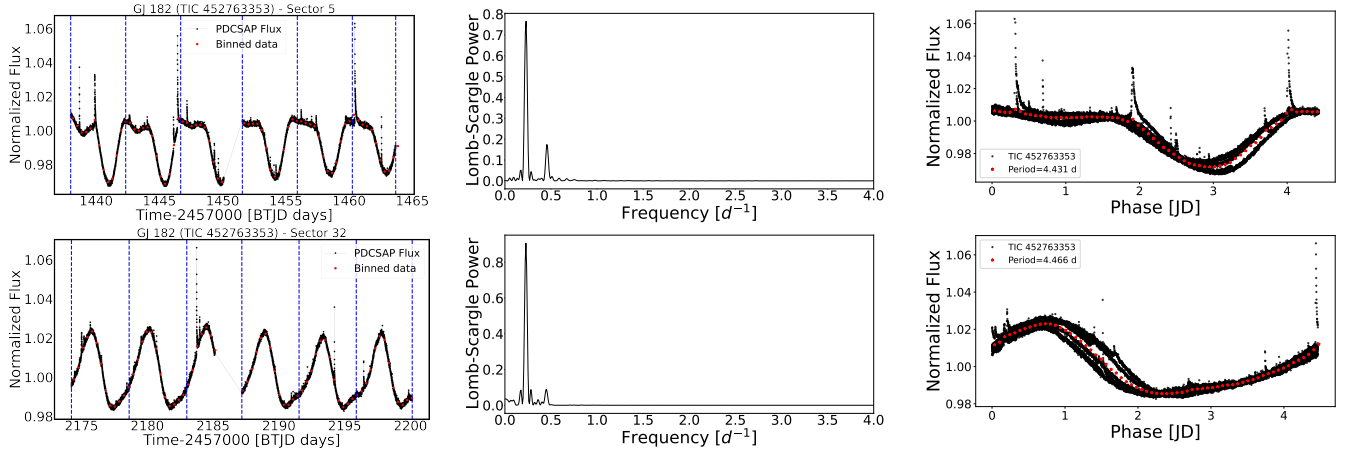


Figure 3. The light curves (left), Lomb-Scargle periodograms (middle) and phase-folded light curves (right) of GJ 182 are shown here for sector 5 (top row) and sector 32 (bottom row). The light curves were binned with intervals of 500 minutes and are shown in red dots and blue dotted lines represent the segments used for starspot modeling in BASSMAN. The right column displays the phase-folded light curves, where the data are folded with the most significant peak obtained from the LS periodogram. The black stars in the phase light curve represent the 100 min binned data. The figure titles in the left column include the object names and sectors. Additionally, the rotation periods of the objects are mentioned within the phase light curves.

same rotational periods within the error bar (Table 2). When we phase-folded the light curve at the most significant peak, they showed significant variability with sinusoidal or semi-sinusoidal structures. Rotational modulation of cold spots with the object is mainly responsible for producing such periodic or quasi-periodic behavior in the light curve. However, by just inspecting the light curve morphology, we cannot find the location of the starspots. To map the distribution of starspots on the star’s surface, a more sophisticated approach is necessary. Starspot modeling or light-curve inversion provides a deeper understanding of the distribution of starspots on the surface of these stars (Ikuta et al. 2020; Bicz et al. 2022; Ikuta et al. 2023).

3.1. GJ 182

GJ 182 has been observed in TESS sector 5 (in November 2018; Camera 1 and CCD 2) and sector 32 (in December 2020; Camera 1 and CCD 2) with roughly two years time gap. The observations were conducted in a 2-min cadence mode and from the light curve we determined the rotation period of 4.35 ± 0.2 and 4.38 ± 0.4 days for this object in Sector 5 and Sector 32 respectively. Previously, Kiraga & Stepien (2007) reported a rotation period of 4.41 d using ASAS photometric data. A comparison of rotation periods with previous studies was mentioned in Table 2. Byrne et al. (1984) suggested that the optical variability of GJ 182 is normally due to the presence of large dark spots on the surface. From the TESS observation, we observed the shape of the light curve between sector 5 and sector 32 changes significantly, which reflects the evolutionary changes in the surface phenomena. To find out the distribution of the starspots in both sectors, the light curve was reconstructed by a two-spot model in both sectors with the inclination angle of 60° (Donati et al. 2008). From the light curve, we rejected outlier points exceeding 0.05σ above the mean and manually removed the parts of flare events from the light curve.

In the case of sector 5, the shape and amplitude of the light curve change significantly in each rotation (Fig 3). In the first half of the LC, there is a dip in each rotation and it diminishes in the second half of the LC. As the variability is not constant over time, we modeled the light curve by dividing it into few individual segments, and each segment contains the full rotation of the object. However, in Sector 5, the 3rd and 6th segments, and in Sector 32, the 3rd segment, do not contain a full rotation period (see left in Fig 3). Consequently, we excluded these incomplete segments from our analysis. It can be allowed to check any spot evolution in the whole LC. We removed the flare events manually using ‘RMPARTS’ command in BASSMAN code from the LC. To estimate the amplitude we used the LC of sector 32 as it has maximum brightness compared to the LC in sector 5. We used the same method as described in Bicz et al. (2022) by phasing the LC and taking the maximum normalized flux value without taking into flare events. In this method, we obtained a maximal amplitude value of 1.024 (see Fig 5 (left)) and used this value for our analysis. Furthermore, to better visualize spot evolution during each rotation, we used the model derived from one rotation as a starting point

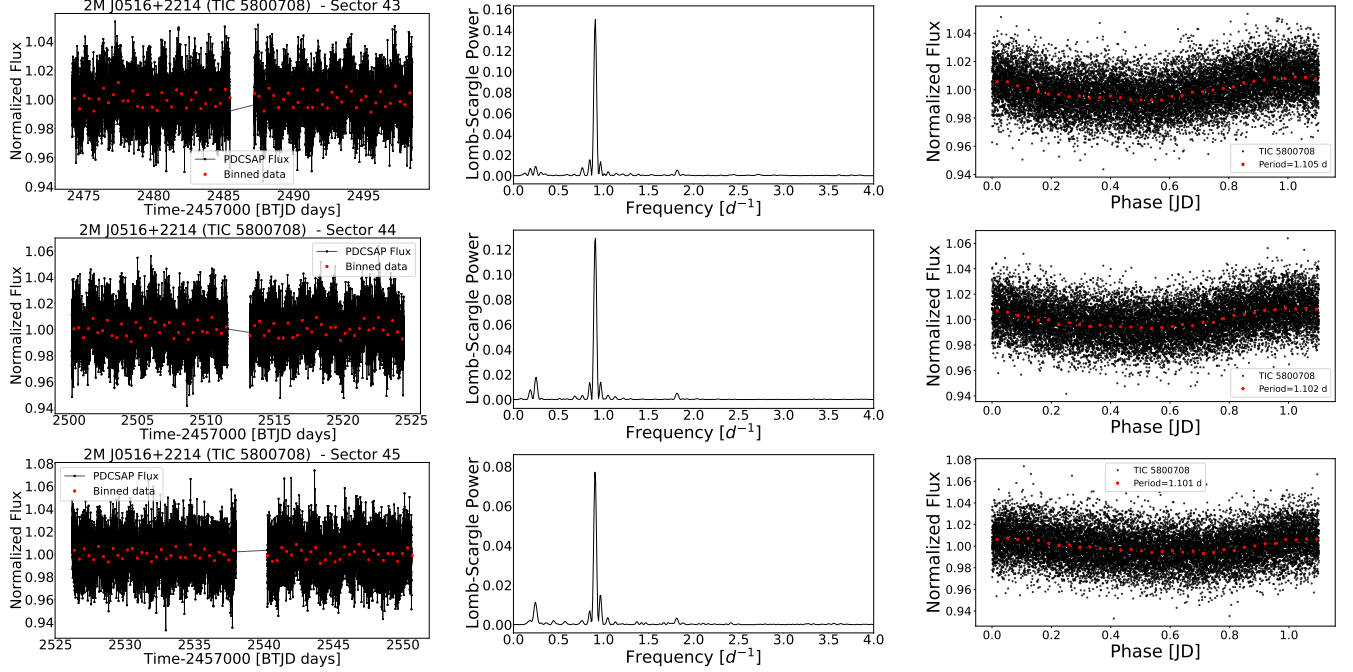


Figure 4. The light curves (left), Lomb-Scargle periodograms (middle) and phase folded light curves (right) of 2MASS J05160212+221452 are shown here for sectors 43 (first row), 44 (second row) and 45 (third row). The light curves were binned with intervals of 500 minutes and are shown in red dots. The right column displays the phase-folded light curves, where the data are folded with the most significant peak obtained from the LS periodogram. The black stars in phase light curve represent the 50 min binned data. The figure titles in the left column include the object names and sectors. Additionally, the rotation periods of the objects are mentioned within the phase light curves.

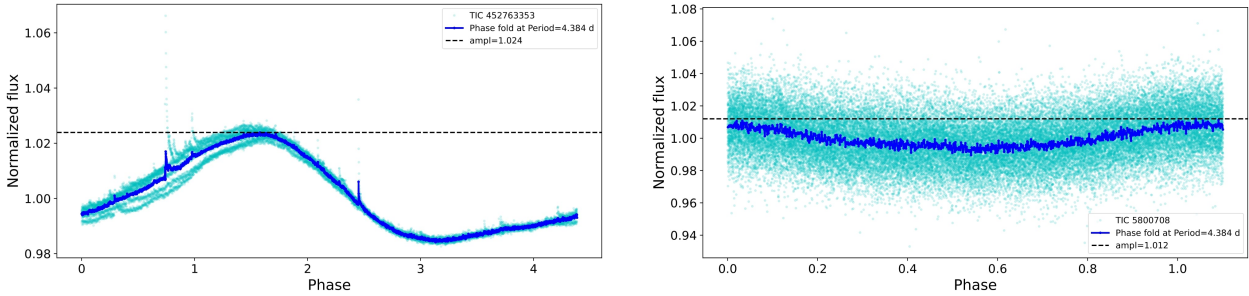


Figure 5. The cyan curve represent the phase light curve of GJ 182 (left) in sector 32 and 2MASS J056+2214 (right) from all sectors. The blue line indicates the binning light curve and the black dashed line shows the estimated maximal amplitude, used for spot modeling.

for the next. Additionally, we applied the value of the differential coefficient of 0.06 ± 0.03 rad/day for our analysis, adopted from [Donati et al. \(2008\)](#). In sector 5, each segment of the LC was reconstructed by a three-spot model with a spot relatively at a higher latitude (ranging $30^\circ - 70^\circ$) and others near the equator. We also tested a two-spot model but it had a lower log-probability value compared to the three-spot model. So, we chose the three-spot model to fit the LCs better. Similarly, in sector 32 we modeled each segment of the LC using both two-spot and three-spot models. Again, the three-spot model was well-fitted to the LCs with higher log-probability values compared to the two-spot model. So, the three-spot model is more reliable for capturing the data from the light curve, with one spot located relatively at a lower-latitude region (ranging from -47° to -55°) whereas the other two were situated at the higher mid-latitude region. Thus, the three-spot model is a more reliable choice in both sectors. The estimated parameters of starspots and comparison with analytic solution are shown in Table 5, Table 6 for sector 5 and in Table 7, Table 8 for sector 32. The figures were decorated in Figure 6 (sector 5) and Figure 7 (sector 32). Note that the reduced chi-square

values greater than 1.0 in Table 6 do not indicate underfit but rather indicate the short-term light fluctuation of the TESS light curves.

In addition, we have also detected 48 flare events within the energy range from 10^{32} to 10^{35} erg and the highest number of flares has energy around 10^{33} erg. Among them, a few of the flares were lasting more than 2.5 hours. The estimated parameters in these flare events are listed in Table 3 and 4. Previously, [Byrne et al. \(1984\)](#) recorded four flare events within the energy range from 10^{32} to 10^{34} erg from the photometric data using the 0.75-m telescope of the South African Astronomical Observatory at Sutherland. We have also discussed the nature of flare events in Section 4.

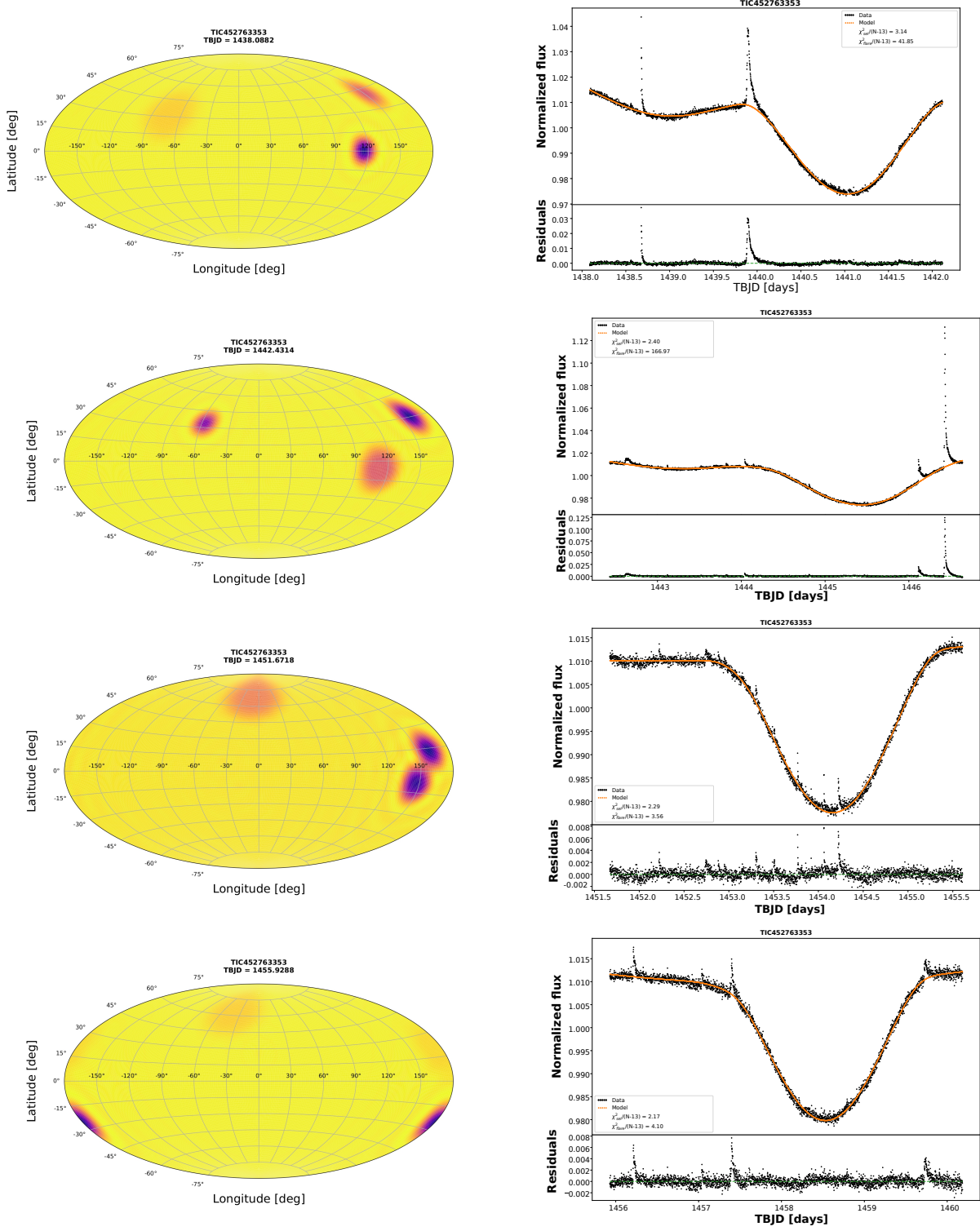


Figure 6. The left column represents the positions, sizes, and contrast of spots in the Aitoff projection (at phase = 0) of GJ 182 in sector 5. The right column shows the observed light curve from TESS (black dots) and the model-fitted light curve (orange curve) along with their residuals and the reduced chi-square written in the corner of the plot. The upper row corresponds to the first modulation of the light curve, while the next bottom row represents the second modulation of the light curve for GJ 182. Additionally, the fourth, and fifth rotations are represented in the third, and fourth rows, respectively.

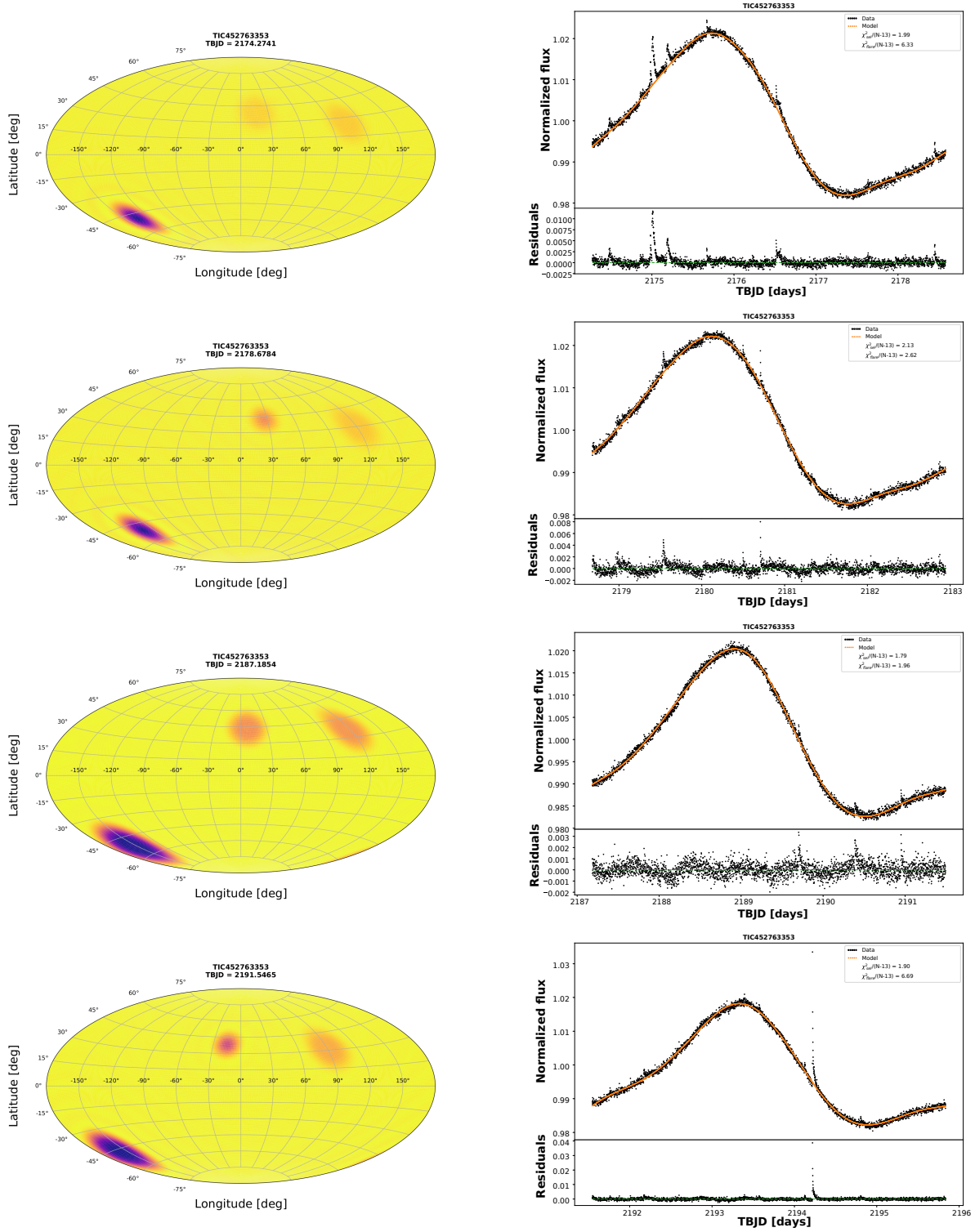


Figure 7. The left column represents the positions, sizes and contrast of spots in the Aitoff projection (at phase = 0) for GJ 182 in sector 32. The right column shows the observed light curve from TESS (black dots) and the model-fitted light curve (orange curve) along with their residuals and the reduced chi-square written in the right corner of the plot. The first, second, fourth, and fifth rotations are represented in the first, second, third, and fourth rows, respectively.

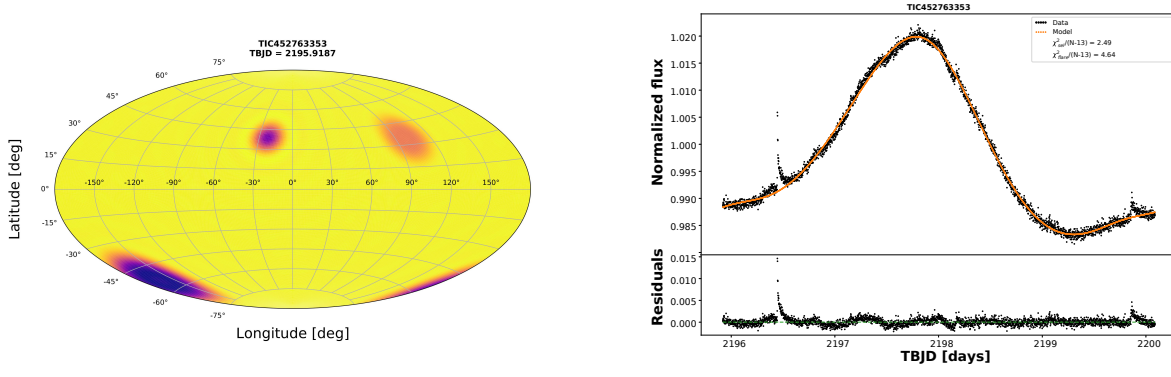


Figure 8. (Continued) This figure represents the sixth rotation of GJ 182 in sector 32.

Table 6. Comparision between model estimated spot parameters and the analytically estimated spot parameters of GJ 182 in sector 5 in each modulation.

Modulation	Analytic Mean Spot Temperature [K]	Model Mean Spot Temperature [K]	Analytical Spot Size [% area of star]	Model Spot Size [% area of star]	SNR	log-Probability	Reduced chi-square
Rotation-1	3176 ± 68	3550	8.98 ± 1.28	7.03	1298	6974	3.14
Rotation-2	3176 ± 68	3214	8.98 ± 1.28	5.15	1483	7502	2.40
Rotation-4	3176 ± 68	3522	8.33 ± 1.19	6.85	1519	7094	2.29
Rotation-5	3176 ± 68	3650	7.93 ± 1.13	8.49	1558	7819	2.18

Table 5. Estimated spots parameters of GJ 182 (sector 5) in this work.

Modulation	Start Time [BTJD]	Stop Time [BTJD]	Lat1 (ϕ_1) [deg]	Lat2 (ϕ_2) [deg]	Lat3 (ϕ_3) [deg]	Initial Long1 (Λ_1) [deg]	Initial Long2 (Λ_2) [deg]	Initial Long3 (Λ_3) [deg]	T_{spot1} [K]	T_{spot2} [K]	T_{spot3} [K]	Size1 [% area of star]	Size2 [% area of star]	Size3 [% area of star]
Rotation-1	1438.09	1442.12	0.06	40.90	30.82	115.23	150.76	-72.22	2656 ± 1089	3030 ± 775	3746 ± 173	1.02	1.04	4.97
Rotation-2	1442.43	1446.64	-6.31	30.00	33.39	111.54	158.23	-57.08	3374 ± 523	2775 ± 1002	3063 ± 750	3.06	1.06	1.04
Rotation-4	1451.67	1455.61	-8.84	13.10	67.67	146.00	160.19	-10.33	3129 ± 645	3137 ± 642	3731 ± 203	1.52	1.28	4.05
Rotation-5	1455.93	1460.18	-25.13	18.27	61.48	179.47	173.68	-39.22	2657 ± 1107	3746 ± 127	3742 ± 182	1.09	3.13	4.27

Table 8. Comparison between model estimated spot parameters and the analytically estimated spot parameters of GJ 182 in sector 32 in each modulation.

Modulation	Analytic Mean Spot Temperature [K]	Model Mean Spot Temperature [K]	Analytical Spot Size [% area of star]	Model Spot Size [% area of star]	SNR	log-Probability	Reduced chi-square
Rotation-1	3176 ± 68	3185	7.56 ± 1.08	6.18	1618	7889	1.98
Rotation-2	3176 ± 68	3029	7.43 ± 1.06	4.95	1564	8294	2.13
Rotation-4	3176 ± 68	3142	7.42 ± 1.06	7.55	1705	8812	1.78
Rotation-5	3176 ± 68	3036	7.49 ± 1.07	5.82	1657	8817	1.90
Rotation-6	3176 ± 68	2980	7.30 ± 1.04	6.04	1444	7902	2.50

Table 7. Estimated spots parameters of GJ 182 (sector 32) in this work.

Modulation	Start Time [BJD]	Stop Time [BJD]	Lat1 (ϕ_1) [deg]	Lat2 (ϕ_2) [deg]	Lat3 (ϕ_3) [deg]	Initial Long1 (Λ_1) [deg]	Initial Long2 (Λ_2) [deg]	Initial Long3 (Λ_3) [deg]	T _{spot1} [K]	T _{spot2} [K]	T _{spot3} [K]	Size1 [% area of star]	Size2 [% area of star]	Size3 [% area of star]
Rotation-1	2174.27	2178.58	37.98	-49.05	25.14	16.44	-136.56	104.69	3334 ± 559	2554 ± 1110	3223 ± 684	2.57	1.09	2.52
Rotation-2	2178.68	2182.94	41.26	-50.90	29.62	25.92	-132.76	119.31	2693 ± 1100	2546 ± 1108	3269 ± 642	1.09	1.13	2.72
Rotation-4	2187.19	2191.49	43.06	-52.27	35.88	6.70	-152.74	116.26	3211 ± 672	2926 ± 1106	3260 ± 631	2.36	2.55	2.65
Rotation-5	2191.55	2195.84	37.70	-47.31	30.73	-15.23	-157.76	89.93	2674 ± 1092	2771 ± 1127	3285 ± 619	1.03	2.02	2.77
Rotation-6	2195.92	2200.09	38.25	-53.87	33.75	-22.66	-163.62	97.89	2679 ± 1085	2946 ± 1102	3124 ± 708	1.03	2.71	2.30

3.2. TIC 5800708 (2M0516+2214)

2M0516+2214 object has been observed in TESS sector 43 (September 2021; Camera 4; CCD 2), sector 44 (October 2021; Camera 2; CCD 1) and sector 45 (November 2021; Camera 1; CCD 4). The light curves obtained from each Sector varied slightly in amplitude, while displaying approximately similar nature in variability (Figure 4). The estimated rotation periods from the LS periodogram are 1.10 days across all sectors. The Gaussian process methods provide rotation periods of 1.101 ± 0.002 d, 1.101 ± 0.001 d, and 1.101 ± 0.004 d of sector 43, 44, and 45 respectively that were precisely similar to the LS periodogram (refer Table 2). This is the first time we have estimated the rotation period for this object. The power spectrum for 2M0516+2214 demonstrated a significant peak centered at this rotation period. Moreover, the phase-folded light curves also appear sinusoidal while folding it on this significant peak, supporting the presence of starspot activity on the stellar surface, depicted in figure 4 which makes it a suitable object for this study. But the LCs of 2M0516+2214 in each sector had large scatter due to statistical noise, making it challenging to construct a reliable spot model. To address this, we first constructed a combined phased LC from all three sectors (43,44, and 45), then modeled the combined phased LC with a two-spot configuration and it strongly suggested the presence of two primary spots (see 1st row of Fig 9). As a result, one spot is located in the lower mid-latitude region (-22°), and the other one is at a higher latitude around 47° , separated by 99.2° . Combining the phased LC from all sectors leads to long-term spot features with a slightly higher signal-to-noise ratio of around 83. Using this combined model as a starting point, we modeled the phased LCs of each sector (43,44, and 45) individually and we obtained a two-spot model for better fit to the LCs. Therefore, the other sectors (43,44 and 45) also showed similar kind of spot distribution. During the model of combined LC, sector 43,44 and 45, the spot1 was situated at 47.5° , 42.9° , 46.5° and 52.3° in latitude respectively whereas spot2 was located at -22.7° , -22.0° , -25.3° and -19.3° in latitude respectively. The spot distribution of the combined phased LC and LC in sector 43,44 and 45 were almost similar. Furthermore, we also recreated the light curve with a three-spot model and obtained a different model and analytical solution of spots' parameters. Apart from that, we also checked for the log-probability (logP) value and found that in the two-spot model logP is relatively higher than in the three-spot model and the model estimated parameters are also close to the analytical solutions. So, we choose the two-spot model for the best fit for 2M J0512+2214. The estimated parameters of starspots have been seen in Table 9 and the mean spot model was listed in Table 10.

Table 10. Comparison between model estimated spot parameters and the analytically estimated spot parameters of 2M0516+2214 in the combined sector as well as sector 43,44 and 45.

Modulation	Analytic Mean Spot Temperature [K]	Model Mean Spot Temperature [K]	Analytical Spot Size [% area of star]	Model Spot Size [% area of star]	SNR	log-Probability	Reduced chi-square
Combined	2752 ± 65	2480	5.40	5.57	82.7	33882	0.71
43	2752 ± 65	2541	5.54	5.59	89.19	11665	0.75
44	2752 ± 65	2584	5.47	4.92	83.8	11417	0.70
45	2752 ± 65	2546	5.15	5.83	75.4	10742	0.69

NOTE—

Table 9. Estimated Spots parameters of 2M0516+2214 of all sectors.

Sector	Start Time [BTJD]	Stop Time [BTJD]	Lat1 (ϕ_1) [deg]	Lat2 (ϕ_2) [deg]	Initial Long1 (Λ_1) [deg]	Initial Long2 (Λ_2) [deg]	T_{spot1} [K]	T_{spot2} [K]	Size1 [% area of star]	Size2 [% area of star]
Combined	2474.17	2550.63	47.46	-22.63	-172.72	-75.18	2787 ± 249	2045 ± 1017	2.64	2.93
43	2474.17	2498.47	42.91	-22.02	-163.05	-68.15	2785 ± 258	2217 ± 913	2.72	2.87
44	2500.19	2524.44	46.51	-25.34	-175.09	-76.77	2782 ± 254	2276 ± 870	2.63	2.28
45	2516.19	2550.63	52.31	-19.29	-167.52	103.77	2833 ± 203	2150 ± 935	2.79	3.03

3.3. Flare Analysis

In this study, we examined the flare events of GJ 182 across two sectors. In sector 5, we identified 25 confirmed flare events and 5 probable events while in sector 32 there were 23 confirmed events and 2 probable events. The parameters of confirmed flare events of GJ 182 are summarised in Table 3 and 4 and the flare energies and duration of the flares are plotted as a histogram in Figure 11. The bottom panel of Figure 10 illustrates the relationship between flare duration and total energy in the log-log plot. The duration was derived by subtracting the start of the flare time from the end of the flare time and the total energy was estimated as described in section 2.3. The plot showed a strong correlation (correlation coefficient ~ 0.97) between these properties which implied that stronger superflares have much longer duration. As a result, a linear positive correlation was found between duration (Δt) and bolometric energy of flares (E_{bol}) i.e. $\Delta t \propto E_{bol}^{0.67 \pm 0.02}$. Generally, the theoretically predicted value of the power-law index of E was 1/3 for the flares on solar-type stars i.e. for magnetic reconnection. Maehara et al. (2015) got 0.39 ± 0.03 . Later, Namekata et al. (2017) found 0.38 ± 0.06 for solar white-light flares. Maehara et al. (2020) again found a positive correlation for YZ CMi with an index of E was 0.21 ± 0.04 which satisfied the magnetic reconnection theory. But for superflares on GJ 182 (M0.5), we obtained a slightly higher value i.e. 0.67 ± 0.02 . Previous studies e.g., Jackman et al. (2021), Tu et al. (2021) have also found slightly diverse values of 0.6 for mid-M dwarfs using NGST and 0.42 for solar-type stars using TESS respectively. For a K2V object, Kepler-411, Araújo & Valio (2021) have reported 0.86 ± 0.03 which is larger than our estimated value.

In addition, the flares occurrences in M-dwarfs follow power-law distribution in energy (Lacy et al. 1976). This distribution is described by the equation,

$$dN(E) = \beta E^{-\alpha} dE dt \quad (9)$$

where N is the number of flares that occurred in the observational period dt , E is the total flare energy, β is a proportionality constant, and α is the power-law index. The power law index α also denotes the slope of the cumulative flare frequency distribution (FFD). Here, we investigated this distribution by plotting the cumulative FFD of all flare events of GJ 182 and fitted it to a power-law model⁹ using Markov Chain Monte Carlo (MCMC) method to find out α and β . For many stars, flare frequency distribution follows the simple power law. Initially, we attempted to fit the flare frequency distribution plot with the whole energy range of the flare but the fit appeared inaccurate at the low energy region. This may be due to the redder wavelength of TESS observation, where low energy flares are less reliably detected in the presence of photometric noise (Doyle et al. 2019; Tu et al. 2021; Vida et al. 2024). Then, the α index may be affected by this energy range used for fitting (Yang et al. 2023). To address this we avoided the initial phase of the horizontal trend at the low energy range of the FFD and used 10^{33} to 10^{35} erg energy range for better fit. As a result, in sector 5, we obtained the power-law index (α) as 1.53 ± 0.12 while 1.86 ± 0.22 for sector 32 in the range of energy from 10^{33} to 10^{35} erg. For comparison, Lin et al. (2019) reported the power-law index as 1.82 ± 0.02 and Yang & Liu (2019) obtained 2.13 ± 0.05 of M-type stars. Similarly, Maehara et al. (2021) found α to be approximately 1.75 ± 0.04 for the flares on M-dwarfs in the energy range between 10^{32} to 10^{34} erg while Yang et al. (2023) also gave $\alpha \sim 1.85 \pm 0.13$. So, our estimated value of α is almost similar within error bar to the obtained value from earlier studies and as $\alpha > -2$ which suggested that the total energy of the flares is mainly dominated by high-energy flare events rather than low-energy (Paudel et al. 2018; Jackman et al. 2021; Gao et al. 2022)

4. DISCUSSION

We analyzed the power spectrum of two young M-dwarfs, GJ 182 and 2M0516+2214 visually and we found that they exhibited a prominently dominated peak (Fig 3, Fig 4). But apart from this large peak, there are relatively weak secondary peaks, also present in a few sectors. In the case of GJ 182, there is a small peak present in sector 5 and it is diminishing in sector 32 LC (middle panel in figure 3). We detected that this secondary peak appears at the harmonic of the primary peak. Similar case for 2M0516+2214, as we go from sector 43 to 45 the power of the second small peak increases. We also calculated the false-alarm probability (FAP) of the main peak for these objects, as determined by the LS algorithm, which was found to be very small ~ 0 . Subsequently, folding the light curves with this main peak, a clear periodic nature emerged (Figure 3, 4). Folding the light curves at the secondary peak does not show any periodic nature; rather it is more scattered. This behaviour was often attributed to the presence of cool spots or spot groups on its surface, which co-rotating with the objects and periodically came in and out of our line of sight (Rebull et al.

⁹ <https://altaipony.readthedocs.io/en/latest/tutorials/ffds.html>

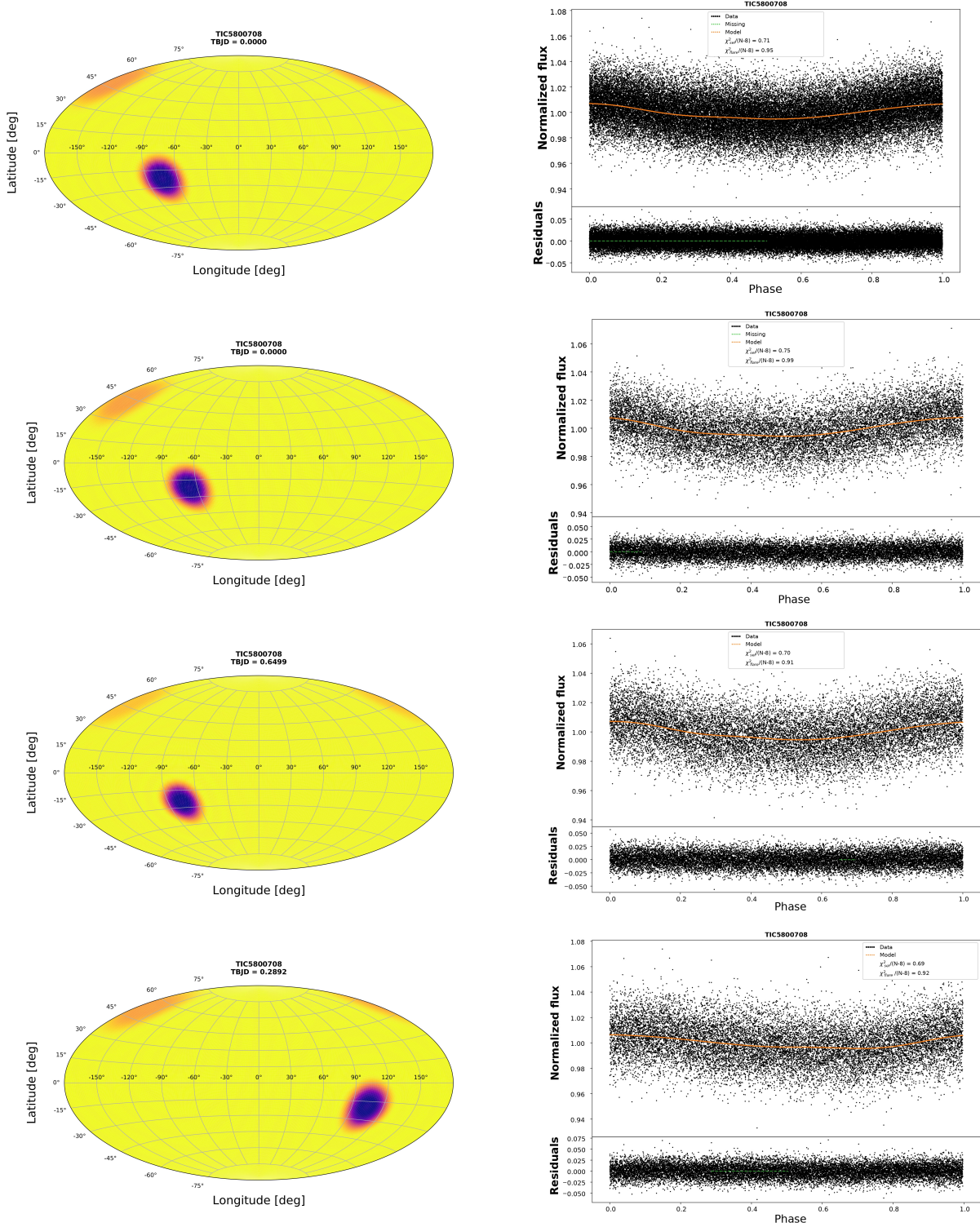


Figure 9. Left column represents the positions, sizes, and contrast of spots in the Aitoff projection (at phase = 0) of 2MASS J05160212+221452. The right column shows the phased light curve from TESS (black dots) and the model-fitted light curve (orange curve) along with their residuals and the reduced chi-square written in the corner of the plot. The upper panels are for combined phase light curve, 2nd panel shown for sector 43, 3rd panels are for sector 44 and the below panels displayed for sector 45 of 2MASS J05160212+221452.

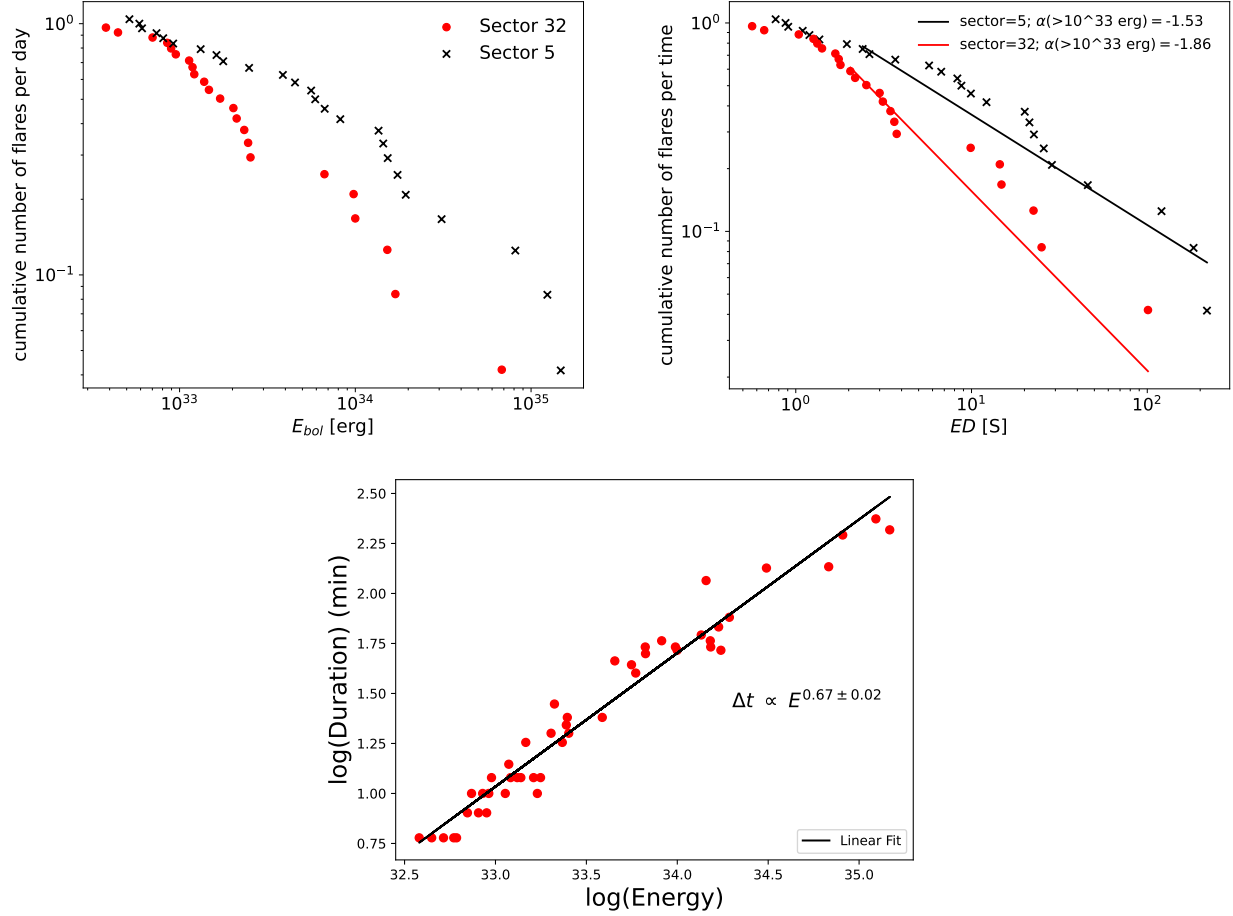


Figure 10. Cumulative flare frequency distributions vs. energy (left panel) and equivalent duration (right panel) for GJ 182 in sectors 5 and 32 are shown here. For a given energy (or equivalent duration) on the x-axis, the cumulative number of flares per day is given on the y-axis. Bottom: Flare duration versus total energy of the flare is shown.

2016a). GJ 182 was observed with an interval of almost two years and it is observed that the shape and amplitude of the light curve also changed significantly (figure 3). In particular, the light curve of GJ 182 changes two to one local minima in one rotation period. In sector 5, GJ 182 showed a double-dip structure in the phase light curve, while in sector 32 the dip disappeared. As a result, the strength of the secondary peak in the LS periodogram (Fig 3) in sector 32 decreases compared to sector 5. Moreover, the shape of the LC changes over the sector but the rotation period remains the same. Such a scenario might arise due to spot/spot group evolution and/or latitudinal differential rotation (Rebull et al. 2016b). Previously, Davenport et al. (2015) also suggested that such double-dip light curves possibly arise due to the spots which are well-separated in longitudes.

We further analyzed and modeled the light curves of these two objects in each sector to study the starspot distribution on the stellar surface, as their brightness variation shows an almost periodic nature. We run the model for each sector individually to check any spot evolution on the surface. In our analysis of the LC in sector 5, we observed a significant change in the amplitude of the LC during each rotation of the object. To investigate the variation we divided the LC into a few segments for modeling and each segment contains one full rotation of the object (discussed in section 3). We found that our modeling on GJ 182 strongly indicates the presence of three spots on the surface. Notably, the spot2 in sector 5 exhibited a consistent shift in longitude from 150.8° to 173.7° across each rotation. While spot1 demonstrated a more significant longitudinal shift, moving from 115.3° to 179.5° . The shiftiness of spot1 is much more than spot2 because of the differential rotation of this object as spot1 is placed near the equator while spot2 is at a higher latitude. Mainly, this spot1 produced the local minima of the LC and the other two spots (mainly spot3) were responsible for the secondary minima. As spot3 moves towards the higher latitude region (30° to 67°)

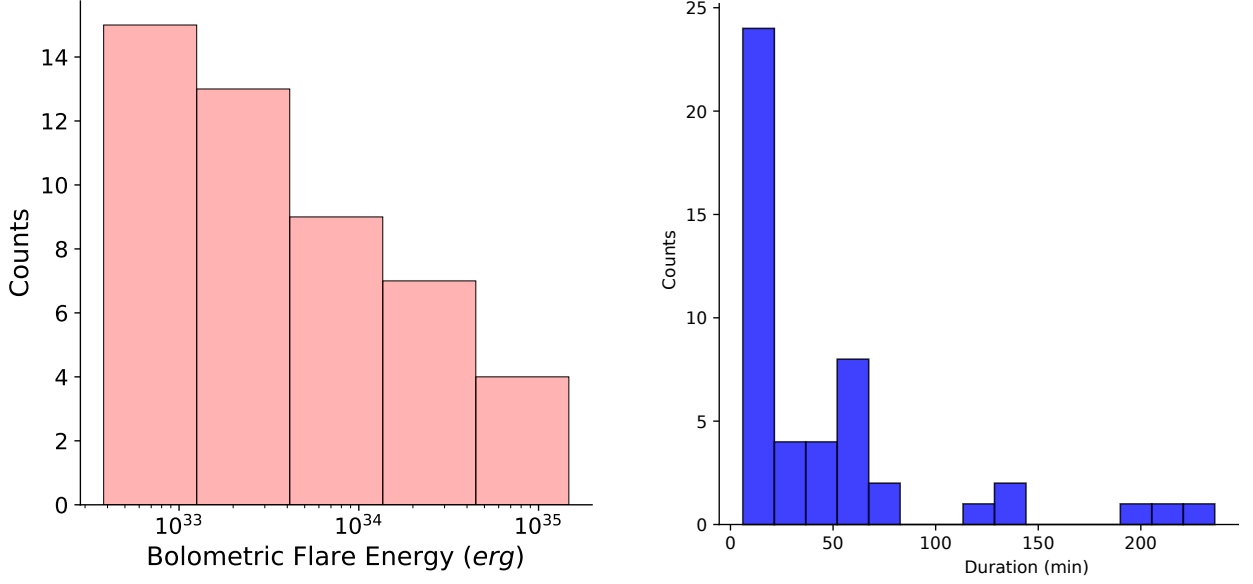


Figure 11. Histograms for the energy (left) and duration (right) of flares of GJ 182 are shown.

during each modulation, consequently the dip in the secondary minima vanishes. Furthermore, the total size of the spot is also varied from 5.15% to 8.49% of the stellar surface during each rotation. Similarly, in sector 32, the LC of each rotation was also reconstructed by a three-spot model. Meanwhile, spot2 migrated to the lower latitude region while the other two spots remained at the mid-latitude region (around 25° to 43°). These mid-latitude spots mainly contribute to the local minima of LC in sector 32. As spot2 goes to the lower latitude region, it can not contribute much to produce minima in the LC. So, the shape of the LC also changes from sector 5 and the dip in the secondary minima completely vanished in sector 32. The total size of the spot also varying 5% to 7.5% during each rotation in sector 32. These findings regarding differential rotation, shifting in longitudes, migrating the spots, as well as dynamic change of spot coverage with time, provide valuable insight into the magnetic activity, revealing a complex interplay of factors that influence the surface features of this object. The spectropolarimetric measurement and surface mapping using Zemman-Doppler imaging of GJ 182 revealed that it has a strong axisymmetric toroidal magnetic field and non-axisymmetric poloidal component (Donati et al. 2008; Lund et al. 2021). The non-axisymmetric poloidal field and 41° deviation of the magnetic axis from the rotation axis (Lang et al. 2012) can cause less stability of stellar spots which might lead to shorter lifetime or exhibit more erratic migration patterns across the stellar surface. The separation between the spots in longitudes also varies in both sectors during each rotation, reflecting the differential rotation for this object. Previously, GJ 182 was confirmed as a differential rotator with a surface angular rotation shear between the equator and poles is $d\Omega = 0.06 \pm 0.03 \text{ rad d}^{-1}$ (Donati et al. 2008). Furthermore, we identified 25 flares in sector 5 while 23 flares in sector 32 and we observed that in sector 5 most of the flare events had greater energy (19 flares had energy $\geq 10^{33} \text{ erg}$). In the case of sector 32, 17 flares had energy $\geq 10^{33} \text{ erg}$. This could be possible due to the change in the magnetic field strength which was already suggested by Donati et al. (2008). Using Stokes V data Donati et al. (2008) observed the longitudinal field variation for this object. Reinert & Basri (2009) also reported the average magnetic field around 2.5 kG from unpolarized spectroscopy. The shape and amplitude of the light curve have changed over two years for this object and can be explained by the evolution of spots and their sizes along with their magnetic field strength. This kind of scenario was also observed in AU Mic and YZ CMi objects reported in (Ikuta et al. 2023). The total spot area relative to the stellar hemisphere varied significantly in two years and the flare frequency remained nearly constant in both sectors ($25/25.987 = 0.96 \text{ day}^{-1}$ in sector 5 and $23/25.589 = 0.90 \text{ day}^{-1}$ in sector 32) although the shape and amplitude of the light curve changed. we obtained a mean spot temperature of approximately 3484 K and 3074 K in sector 5 and 32 respectively and an average spottedness varied from 5% to 8.5% across sectors 5 and 32 for three-spot modelling (Table 6 and 8).

For 2M0516+2214, the visual inspection of the smooth periodic variation in the LCs of all sectors strongly indicated the presence of two primary spots on the surface. However, the LCs exhibited significant scatter due to statistical

noise. Two-spot model for this object reveals that it had a high-latitude spot along with a spot in the lower mid-latitude region. However we observed a significant shift in the longitude of spot2 in sector 45, although their size remained consistent at approximately 5.4%. As the inclination angle of this object is 24.48° , the local minima of the LC can primarily be attributed to the mid-latitude spot. The signal-to-noise ratio (SNR) of the analyzed LCs is 89, 83 and 75 for sectors 43, 44, and 45 respectively. These values are slightly lower than the ideal SNR of 86 required for accurate reconstruction using the BASSMAN algorithm (Bicz et al. 2022). This low value of the SNR complicates the analysis for finding the accurate position of the starspots. Although we got a slightly higher SNR value from the borderline SNR for the modeling in combined phased LC and the sector 43 and we obtained a similar kind of spot distribution in across the sectors. Lower SNR value might be caused of the shift of the position of starspots (Bicz et al. 2022). The fully understand the behavior of shift in longitudes/latitudes of the spots, we need high-resolution temporal data with less statistical noise. From the two-spot modeling of 2M0516+2214, we obtained a mean spot temperature of approximately 2631 K and average spottedness of around 5.42% in sectors 43, 44, and 45. The estimated spot parameters and comparison with the analytical solution are listed in Table 9, 10.

4.1. Flare Analysis

In addition, we have detected 48 flare events of GJ 182 and about most of the flares (35 out of 48 events) are in the superflare category (greater than 10^{32} erg) which indicates GJ 182 is a magnetically active object. From visual Inspection among 48 flares, we identified one “flat-top” flare event, 6 classical flares, and 17 flares that exhibited a complex nature by showing a “peak-bump” profile. Additionally, the other 7 flares showed complex substructures during the rise phase. The remaining flare may have shown less clear features that might be an issue with insufficient temporal resolution. To better understand these structures, 20s cadence data would be beneficial, as it could reveal more details of these events. Apart from these several flares showed multiple peak emissions. However, we could not categorize these events due to their complexity. The “flat-top” flare exhibited a fast rise and then relatively constant emission levels at peak (see Figure 17) and then again exponential decay (Howard & MacGregor 2022). The duration of the constant peaks lasts from a few seconds to minutes. Previously, Jackman et al. (2021) reported a few flat-top flares for low-mass stars using 13-sec cadence data from the Next Generation Transit Survey (NGTS). Using a 20-s cadence of TESS data of low-mass flare stars, Howard & MacGregor (2022) classified 24 flares exhibiting flat-top morphology. Such flares might result from the superposition of multiple unresolved peaks within a single event (Howard & MacGregor 2022) or when quasiperiodic pulsations are unresolved, they can contribute to the flat-top morphology in some flares (e.g., Jackman et al. (2019)). They can also arise from a prolonged-emission event (Howard & MacGregor 2022). In the peak-bump morphology of flares, there is a steeper rise and shallower decay but hump/humps were present in the decay phase (Davenport et al. 2014) (see Figure 16). Peak-bump flare emission is possible due to a cascade of smaller reconnection events or random superposition of two sympathetic flares from the same or nearby active regions (Hawley et al. 2014; Davenport 2016; Howard & MacGregor 2022). Such peak-bump flares have been previously observed e.g., (Günther et al. 2020; Jackman et al. 2021; Howard & MacGregor 2022). Moreover, these complex types of flares have a longer duration (52 min-165 min) as well as higher energy (10^{33} - 10^{34}). A few flares also showed complex emission during the rise phase. Such rise-phase complexity in flare is also observed on the Sun, where accelerated electrons heat the lower atmospheric layers in nearby emission regions. But these processes do not occur simultaneously or with identical intensity (Veronig et al. 2010; Howard & MacGregor 2022). The histogram plot of the flare energy distribution (Figure 11) of GJ 182 showed that most of the flare emitted in the higher energy range, ie $10^{33} - 10^{34}$ erg. As the TESS filter is more sensitive to objects with low temperatures, we obtained the overall energy distribution in the superflare region. In Section 3.3, we obtained the value of the power-law index α of GJ 182 in both sectors through cumulative FFD. Consistent with previous work for M-dwarfs (mentioned in section 3.3), our obtained value of α (1.53 ± 0.12 in sector 5 and 1.86 ± 0.22 in sector 32) matches quite well. Figure 10; (bottom) showed the strong correlation between the durations and the energy of the superflares in our data set in the energy range 10^{32} to 10^{35} erg. Here, the observational value of the power-law index in the duration vs energy plot from TESS was 0.67 ± 0.02 which is slightly larger than the theoretical prediction ($\beta \sim 1/3$). Since this value is derived from the theory of magnetic reconnection for the solar-type flares, it may not precisely illustrate the superflares in the M-dwarfs (Tu et al. 2020). Other literature (mentioned in section 3.3) also reported a slightly higher value and pointed out that one reason may be different spectral types or their different coronal magnetic field strength (Maehara et al. 2015). Another reason may be due to the length of the flare loop of the largest flare is comparable to the solar radius as flare loop length is correlated with the electron temperature and emission measure of the stellar flares (Shibata &

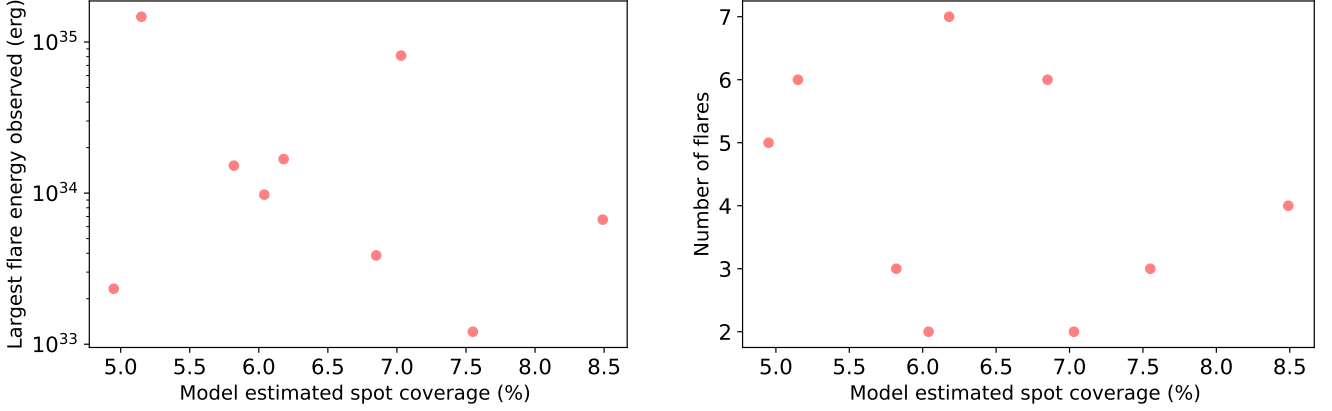


Figure 12. The relationship between rotational phase and flare energy for sector 5 (left) and sector 32 (right) for GJ 182. It is to be noted that no correlation was found between them.

Yokoyama 1999). This strong correlation between duration and flare energy also indicates that strong superflares last longer than their lower energy counterparts (Araújo & Valio 2021).

4.2. Starspot Area and Stellar Flares

It is generally believed that the nature of solar flares and superflares on solar-type stars are caused by the same physical process i.e. magnetic reconnection (Maehara et al. 2015). This suggests that the largest flare may be associated with the largest starspots. Therefore, we examine the correlation between stellar spot coverage and the flares' number and energy to investigate whether the fact is observed. From the spot modeling of GJ 182, we observed that the area of the spots are changing during each rotation. To check the correlation we identified the highest-energy flare and the total number of flares occurring during each rotation. Initially, we plotted our model's estimated spot coverage in each rotation with the largest flare energy observed during each modulation. However, there is no relation found and there is an overall large scatter among them (see figure 12). We further test statistically using the Pearson correlation coefficient (P) which indicates a lack of any correlation with a value, of $P=-0.33$. Further, we look at the number of flares as a function of spot coverage. Again tested with Pearson coefficient correlation and did not find any linear correlation among them ($P=-0.29$). As there is less number data coverage on the spot area, this may contribute to these discrepancies. A more dataset on the time-series photometry of GJ 182 could reveal a deeper insight into this relationship. Furthermore, we again examined the correlation between the bolometric energy of flares and the rotational phase of GJ 182. It could be expected that more and larger flares will occur where there is a concentration of spots, particularly at the phase corresponding to the minimum flux. However, as illustrated in Figure 13, no significant relationship was apparent. The lack of correlation between spots and flares is suspected to occur in fully convective stars (Roettenbacher & Vida 2018). Additionally, for such stars, an anticorrelation between flares and spots has also been shown Bicz et al. (2022), where the magnetic field may be potential. A potential magnetic field has no free magnetic energy to be released during the flare (Aschwanden 2005). Furthermore, Hawley et al. (2014) and Morin et al. (2008) demonstrated that flares on active M dwarfs appear randomly across many independent active regions.

5. SUMMARY

We conducted starspot modeling of *TESS* light curves of two young M-dwarfs, GJ 182 (M0.5) and 2M0516+2214 (M4.5), using *BASSMAN* software to investigate the starspots distribution on the stellar surface and find out the spot properties. Our main results can be summarized as follows:

1. We measured the rotation period of the two objects using the Lomb-Scargle periodogram and Gaussian regression process. GJ 182 has a rotation period of 4.348 ± 0.016 days in sector 5 and 4.384 ± 0.042 days in sector 32, which agrees with the previous studies within the error bar. For the first time, we have estimated the rotation period 2M0516+2214 of 1.102 ± 0.004 days and the rotation period estimated from both methods matches well.
2. The *TESS* light curves of our selected two young M-dwarfs i.e. GJ 182 and 2MASS J05160212+2214528 were reconstructed by *BASSMAN* software. For GJ 182, a three-spot model effectively described the light curves,

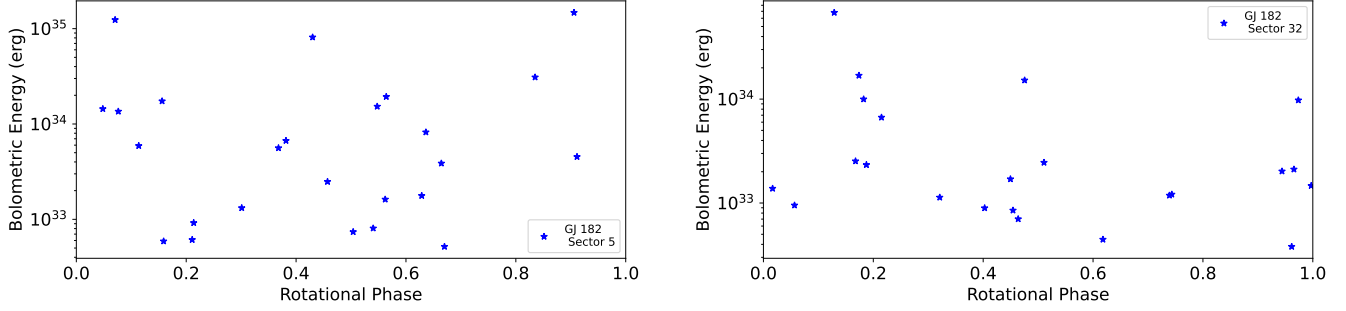


Figure 13. The relationship between rotational phase and flare energy for sector 5 (left) and sector 32 (right) for GJ 182. It is to be noted that no correlation was found between them.

while a two-spot model was suitable for 2MASS J05160212+2214528. To understand better visualization of starspot evolution we divided the LCs of GJ 182 into several segments, each representing full rotation of the object and all segments were well reconstructed by the three-spot model.

3. For GJ 182, we estimated the mean spot temperature to be approximately 3484 K in sector 5 and 3074 K in sector 32 and spottedness varying from 5 % - 8.5 % of the stellar surface and for 2MASS J05160212+2214528 we obtained mean spot temperature around 2541 K - 2759 K and average spottedness about 5.4 %.
4. A total of 48 flare events with bolometric energies between 3.81×10^{32} and 1.47×10^{35} erg from GJ 182 were detected. Further, we have estimated the flare energy within the TESS band, ranging from 8.27×10^{31} to 6.81×10^{33} erg. Moreover, to produce such flare events we have also calculated the lower limit of the magnetic field from 12 G to 232 G. Among 48 flare events, we identified six flares that had a classical shape, only one flare showed flat-top structure, and most of them (17) were categorized as peak-bump flares. Moreover, we also identified 7 flares that showed rise-phase complexity. Moreover, we also conduct an analysis of the starspot area and flare, but could not find any kind of significant correlation among them.
5. For the flares, a strong correlation was found between bolometric flare energy and the duration of the flare with a slope $= 0.67 \pm 0.02$, showing that larger flares last longer and support the magnetic reconnection theory like solar flares.
6. The slope of FFD for GJ 182 is measured to be $\alpha = -1.53 \pm 0.12$ in sector 5 and $\alpha = -1.86 \pm 0.22$ in sector 32 in the energy range 10^{33} to 10^{35} erg and agree well with previous findings for other M-dwarfs. This value also indicated that the total energy of the flare was dominated by high-energy flare events. Further, the rotational phase of GJ 182 did not show any correlation with the flare energy.

6. ACKNOWLEDGMENTS

The authors would like to thank the anonymous referee for the helpful comments and suggestions that significantly improved the paper. This research work is supported by the S N Bose National Centre For Basic Sciences under the Department of Science and Technology, Govt. of India. This paper includes data collected by the TESS mission. Funding for the TESS mission is provided by the NASA's Science Mission Directorate. Funding for the TESS mission is provided by the NASA Explorer Program. STScI is operated by the Association of Universities for Research in Astronomy, Inc., under NASA contract NAS 5-26555. R.K. is grateful to the Department of Science and Technology (DST), Govt. of India, for their INSPIRE Fellowship scheme. RK is thankful to Kamil Bicz for valuable discussions regarding BASSMAN software.

Facilities: TESS

Software: Python 3 (Van Rossum & Drake 2009), astropy (Astropy Collaboration et al. 2013b, 2018b), BASSMAN (Bicz et al. 2022), Altaire (Ilin 2021), Starspot (Angus et al. 2018), matplotlib (Hunter 2007), numpy (Harris et al. 2020), lightkurve (Lightkurve Collaboration et al. 2018).

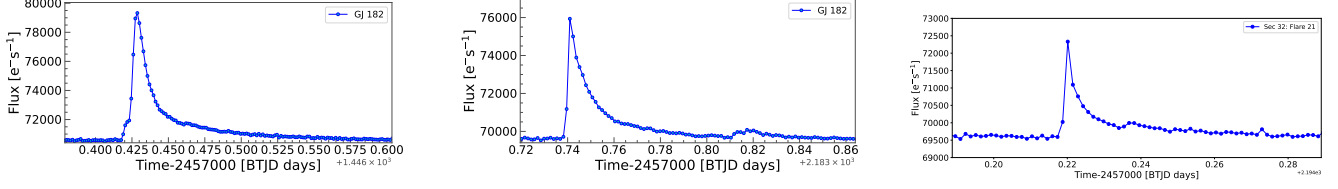


Figure 14. Examples of classical flare events are shown here which have fast rise and slow exponential decay. Out of 48 flares, 6 are in classical shape.

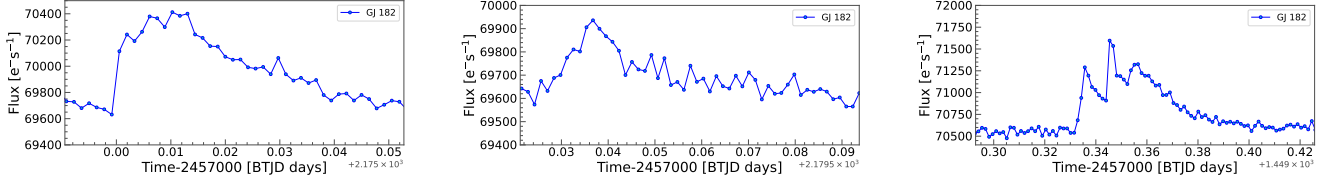


Figure 15. Examples of rise phase complexity flare events with a complex nature in the rise phase are shown here.

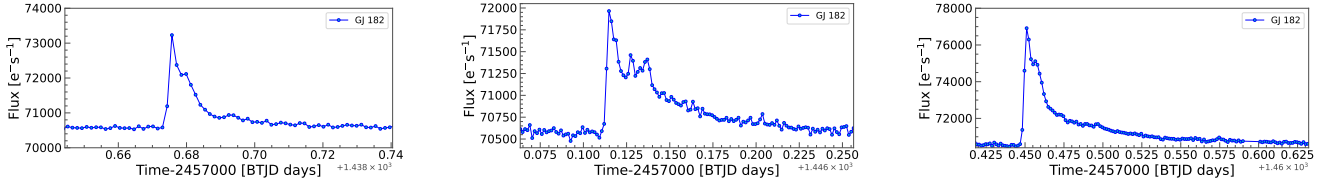


Figure 16. Nearly 17 out of 48 flare events show complex substructure during decay. They are categorized as peak-bump flares. For example we have shown three of them.

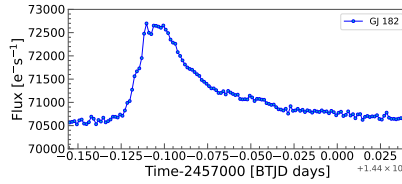


Figure 17. Only one flare has a flat-top structure with a high level of impulsive rise phase and before decaying there is a constant emission level at the peak brightness.

7. DATA AVAILABILITY

The TESS data presented in this article were obtained from the Mikulski Archive for Space Telescopes (MAST) at the Space Telescope Science Institute. The specific observations analyzed can be accessed via [doi: 10.17909/jp7k-qy50](https://doi.org/10.17909/jp7k-qy50).

APPENDIX

A. APPENDIX INFORMATION

REFERENCES

- Akeson, R. L., Chen, X., Ciardi, D., et al. 2013, *PASP*, 125, 989, doi: [10.1086/672273](https://doi.org/10.1086/672273)
- Allard, F., Homeier, D., & Freytag, B. 2012, *Philosophical Transactions of the Royal Society of London Series A*, 370, 2765, doi: [10.1098/rsta.2011.0269](https://doi.org/10.1098/rsta.2011.0269)

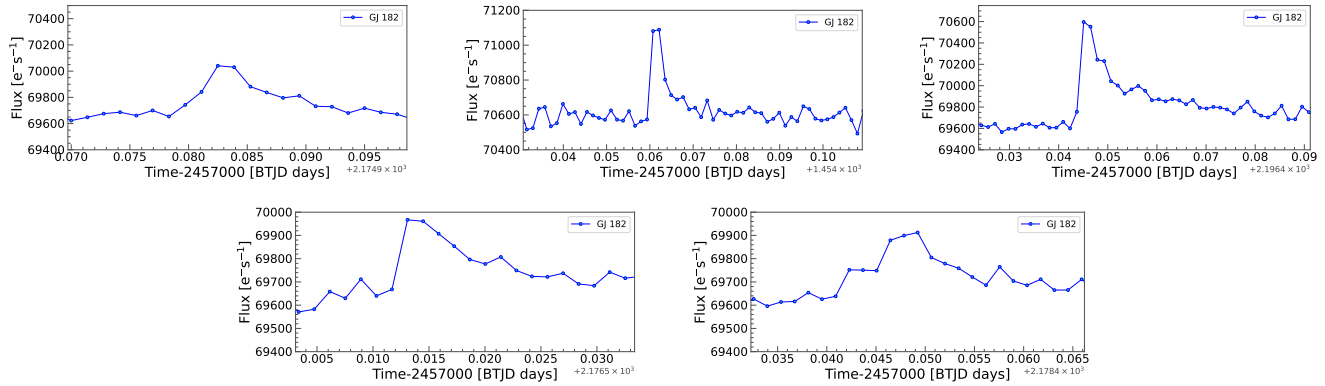


Figure 18. A few flares have insufficient temporal resolution.

- Angus, R., Morton, T., Aigrain, S., Foreman-Mackey, D., & Rajpaul, V. 2018, *MNRAS*, 474, 2094, doi: [10.1093/mnras/stx2109](https://doi.org/10.1093/mnras/stx2109)
- Araújo, A., & Valio, A. 2021, *ApJL*, 922, L23, doi: [10.3847/2041-8213/ac3767](https://doi.org/10.3847/2041-8213/ac3767)
- Aschwanden, M. J. 2005, *Physics of the Solar Corona. An Introduction with Problems and Solutions* (2nd edition)
- Astropy Collaboration, Robitaille, T. P., Tollerud, E. J., et al. 2013a, *A&A*, 558, A33, doi: [10.1051/0004-6361/201322068](https://doi.org/10.1051/0004-6361/201322068)
- . 2013b, *A&A*, 558, A33, doi: [10.1051/0004-6361/201322068](https://doi.org/10.1051/0004-6361/201322068)
- Astropy Collaboration, Price-Whelan, A. M., Sipőcz, B. M., et al. 2018a, *AJ*, 156, 123, doi: [10.3847/1538-3881/aabc4f](https://doi.org/10.3847/1538-3881/aabc4f)
- . 2018b, *AJ*, 156, 123, doi: [10.3847/1538-3881/aabc4f](https://doi.org/10.3847/1538-3881/aabc4f)
- Aulanier, G., Démoulin, P., Schrijver, C. J., et al. 2013, *A&A*, 549, A66, doi: [10.1051/0004-6361/201220406](https://doi.org/10.1051/0004-6361/201220406)
- Bailer-Jones, C. A. L., Rybizki, J., Fouesneau, M., Mantelet, G., & Andrae, R. 2018, *AJ*, 156, 58, doi: [10.3847/1538-3881/aabc21](https://doi.org/10.3847/1538-3881/aabc21)
- Bicz, K., Falewicz, R., Pietras, M., Siarkowski, M., & Preś, P. 2022, *ApJ*, 935, 102, doi: [10.3847/1538-4357/ac7ab3](https://doi.org/10.3847/1538-4357/ac7ab3)
- Byrne, P. B., Doyle, J. G., & Butler, C. J. 1984, *MNRAS*, 206, 907, doi: [10.1093/mnras/206.4.907](https://doi.org/10.1093/mnras/206.4.907)
- Chang, S. W., Byun, Y. I., & Hartman, J. D. 2015, *ApJ*, 814, 35, doi: [10.1088/0004-637X/814/1/35](https://doi.org/10.1088/0004-637X/814/1/35)
- Choudhuri, A. R. 2017, *Science China Physics, Mechanics, and Astronomy*, 60, 19601, doi: [10.1007/s11433-016-0413-7](https://doi.org/10.1007/s11433-016-0413-7)
- Cutri, R. M., Skrutskie, M. F., van Dyk, S., et al. 2003, *VizieR Online Data Catalog*, II/246
- Davenport, J. 2015, PhD thesis, University of Washington, Seattle
- Davenport, J. R. A. 2016, in *Solar and Stellar Flares and their Effects on Planets*, ed. A. G. Kosovichev, S. L. Hawley, & P. Heinzel, Vol. 320, 128–133, doi: [10.1017/S174392131600867X](https://doi.org/10.1017/S174392131600867X)
- Davenport, J. R. A., Hebb, L., & Hawley, S. L. 2015, *ApJ*, 806, 212, doi: [10.1088/0004-637X/806/2/212](https://doi.org/10.1088/0004-637X/806/2/212)
- Davenport, J. R. A., Hawley, S. L., Hebb, L., et al. 2014, *ApJ*, 797, 122, doi: [10.1088/0004-637X/797/2/122](https://doi.org/10.1088/0004-637X/797/2/122)
- Donati, J. F., Morin, J., Petit, P., et al. 2008, *MNRAS*, 390, 545, doi: [10.1111/j.1365-2966.2008.13799.x](https://doi.org/10.1111/j.1365-2966.2008.13799.x)
- Doyle, L., Ramsay, G., Doyle, J. G., & Wu, K. 2019, *MNRAS*, 489, 437, doi: [10.1093/mnras/stz2205](https://doi.org/10.1093/mnras/stz2205)
- Favata, F., Micela, G., Sciortino, S., & D’Antona, F. 1998, *A&A*, 335, 218
- Foreman-Mackey, D. 2018, *Research Notes of the American Astronomical Society*, 2, 31, doi: [10.3847/2515-5172/aaaf6c](https://doi.org/10.3847/2515-5172/aaaf6c)
- Foreman-Mackey, D., Agol, E., Ambikasaran, S., & Angus, R. 2017a, *AJ*, 154, 220, doi: [10.3847/1538-3881/aa9332](https://doi.org/10.3847/1538-3881/aa9332)
- . 2017b, *AJ*, 154, 220, doi: [10.3847/1538-3881/aa9332](https://doi.org/10.3847/1538-3881/aa9332)
- Foreman-Mackey, D., Luger, R., Agol, E., et al. 2021, *arXiv e-prints*, arXiv:2105.01994, <https://arxiv.org/abs/2105.01994>
- Gao, D.-Y., Liu, H.-G., Yang, M., & Zhou, J.-L. 2022, *AJ*, 164, 213, doi: [10.3847/1538-3881/ac937e](https://doi.org/10.3847/1538-3881/ac937e)
- Gilliland, R. L., & Dupree, A. K. 1996, *ApJL*, 463, L29, doi: [10.1086/310043](https://doi.org/10.1086/310043)
- Günther, M. N., Zhan, Z., Seager, S., et al. 2020, *AJ*, 159, 60, doi: [10.3847/1538-3881/ab5d3a](https://doi.org/10.3847/1538-3881/ab5d3a)
- Harris, C. R., Millman, K. J., van der Walt, S. J., et al. 2020, *Nature*, 585, 357, doi: [10.1038/s41586-020-2649-2](https://doi.org/10.1038/s41586-020-2649-2)
- Hawley, S. L., Davenport, J. R. A., Kowalski, A. F., et al. 2014, *ApJ*, 797, 121, doi: [10.1088/0004-637X/797/2/121](https://doi.org/10.1088/0004-637X/797/2/121)
- Hendry, M. A., Bryce, H. M., & Valls-Gabaud, D. 2002, *MNRAS*, 335, 539, doi: [10.1046/j.1365-8711.2002.05496.x](https://doi.org/10.1046/j.1365-8711.2002.05496.x)
- Henry, G. W., Eaton, J. A., Hamer, J., & Hall, D. S. 1995, *ApJS*, 97, 513, doi: [10.1086/192149](https://doi.org/10.1086/192149)
- Hecceg, G. J., & Hillenbrand, L. A. 2014, *ApJ*, 786, 97, doi: [10.1088/0004-637X/786/2/97](https://doi.org/10.1088/0004-637X/786/2/97)
- Heyrovský, D., & Sasselov, D. 2000, *ApJ*, 529, 69, doi: [10.1086/308270](https://doi.org/10.1086/308270)

- Howard, W. S., & MacGregor, M. A. 2022, *ApJ*, 926, 204, doi: [10.3847/1538-4357/ac426e](https://doi.org/10.3847/1538-4357/ac426e)
- Howard, W. S., Tilley, M. A., Corbett, H., et al. 2018, *ApJL*, 860, L30, doi: [10.3847/2041-8213/aacaf3](https://doi.org/10.3847/2041-8213/aacaf3)
- Hunter, J. D. 2007, *Computing in Science and Engineering*, 9, 90, doi: [10.1109/MCSE.2007.55](https://doi.org/10.1109/MCSE.2007.55)
- Ibanez Bustos, R. V., Buccino, A. P., Flores, M., Martinez, C. F., & Mauas, P. J. D. 2023, *A&A*, 672, A37, doi: [10.1051/0004-6361/202245352](https://doi.org/10.1051/0004-6361/202245352)
- Ikuta, K., Namekata, K., Notsu, Y., et al. 2023, *ApJ*, 948, 64, doi: [10.3847/1538-4357/acbd36](https://doi.org/10.3847/1538-4357/acbd36)
- Ikuta, K., Maehara, H., Notsu, Y., et al. 2020, *ApJ*, 902, 73, doi: [10.3847/1538-4357/abae5f](https://doi.org/10.3847/1538-4357/abae5f)
- Ilin, E. 2021, *The Journal of Open Source Software*, 6, 2845, doi: [10.21105/joss.02845](https://doi.org/10.21105/joss.02845)
- Ilin, E., & Poppenhaeger, K. 2022, *MNRAS*, 513, 4579, doi: [10.1093/mnras/stac1232](https://doi.org/10.1093/mnras/stac1232)
- Irwin, J., Berta, Z. K., Burke, C. J., et al. 2011, *ApJ*, 727, 56, doi: [10.1088/0004-637X/727/1/56](https://doi.org/10.1088/0004-637X/727/1/56)
- Jackman, J. A. G., Wheatley, P. J., Pugh, C. E., et al. 2019, *MNRAS*, 482, 5553, doi: [10.1093/mnras/sty3036](https://doi.org/10.1093/mnras/sty3036)
- Jackman, J. A. G., Wheatley, P. J., Acton, J. S., et al. 2021, *MNRAS*, 504, 3246, doi: [10.1093/mnras/stab979](https://doi.org/10.1093/mnras/stab979)
- Jenkins, J. M., Twicken, J. D., McCauliff, S., et al. 2016, in *Society of Photo-Optical Instrumentation Engineers (SPIE) Conference Series*, Vol. 9913, *Software and Cyberinfrastructure for Astronomy IV*, ed. G. Chiozzi & J. C. Guzman, 99133E, doi: [10.1117/12.2233418](https://doi.org/10.1117/12.2233418)
- Johns-Krull, C. M., & Valenti, J. A. 1996, *ApJL*, 459, L95, doi: [10.1086/309954](https://doi.org/10.1086/309954)
- Kiraga, M., & Stepien, K. 2007, *AcA*, 57, 149, doi: [10.48550/arXiv.0707.2577](https://doi.org/10.48550/arXiv.0707.2577)
- Kochukhov, O. 2021, *A&A Rv*, 29, 1, doi: [10.1007/s00159-020-00130-3](https://doi.org/10.1007/s00159-020-00130-3)
- Kovári, Z., Vilardell, F., Ribas, I., et al. 2007, *Astronomische Nachrichten*, 328, 904, doi: [10.1002/asna.200710756](https://doi.org/10.1002/asna.200710756)
- Kowalski, A. F., Hawley, S. L., Wisniewski, J. P., et al. 2013, *ApJS*, 207, 15, doi: [10.1088/0067-0049/207/1/15](https://doi.org/10.1088/0067-0049/207/1/15)
- Kraus, A. L., Herczeg, G. J., Rizzuto, A. C., et al. 2017, *ApJ*, 838, 150, doi: [10.3847/1538-4357/aa62a0](https://doi.org/10.3847/1538-4357/aa62a0)
- Kumbhakar, R., Mondal, S., Ghosh, S., & Ram, D. 2023, *ApJ*, 955, 18, doi: [10.3847/1538-4357/aceb65](https://doi.org/10.3847/1538-4357/aceb65)
- Lacy, C. H., Moffett, T. J., & Evans, D. S. 1976, *ApJS*, 30, 85, doi: [10.1086/190358](https://doi.org/10.1086/190358)
- Lang, P., Jardine, M., Donati, J.-F., Morin, J., & Vidotto, A. 2012, *MNRAS*, 424, 1077, doi: [10.1111/j.1365-2966.2012.21288.x](https://doi.org/10.1111/j.1365-2966.2012.21288.x)
- Lightkurve Collaboration, Cardoso, J. V. d. M., Hedges, C., et al. 2018, *Lightkurve: Kepler and TESS time series analysis in Python*, *Astrophysics Source Code Library*, record ascl:1812.013. <http://ascl.net/1812.013>
- Lin, C. L., Ip, W. H., Hou, W. C., Huang, L. C., & Chang, H. Y. 2019, *ApJ*, 873, 97, doi: [10.3847/1538-4357/ab041c](https://doi.org/10.3847/1538-4357/ab041c)
- Lomb, N. R. 1976, *Ap&SS*, 39, 447, doi: [10.1007/BF00648343](https://doi.org/10.1007/BF00648343)
- Lund, K., Jardine, M., Russell, A. J. B., et al. 2021, *MNRAS*, 502, 4903, doi: [10.1093/mnras/stab305](https://doi.org/10.1093/mnras/stab305)
- Maehara, H., Shibayama, T., Notsu, Y., et al. 2015, *Earth, Planets and Space*, 67, 59, doi: [10.1186/s40623-015-0217-z](https://doi.org/10.1186/s40623-015-0217-z)
- Maehara, H., Notsu, Y., Namekata, K., et al. 2020, *Publications of the Astronomical Society of Japan*, 73, 44, doi: [10.1093/pasj/psaa098](https://doi.org/10.1093/pasj/psaa098)
- Maehara, H., Notsu, Y., Namekata, K., et al. 2021, *PASJ*, 73, 44, doi: [10.1093/pasj/psaa098](https://doi.org/10.1093/pasj/psaa098)
- Magaudua, E., Stelzer, B., Covey, K., et al. 2020, *A&A*, 638, A20, doi: [10.1051/0004-6361/201937408](https://doi.org/10.1051/0004-6361/201937408)
- Messina, S., & Guinan, E. F. 2002, *A&A*, 393, 225, doi: [10.1051/0004-6361:20021000](https://doi.org/10.1051/0004-6361:20021000)
- Messina, S., Millward, M., Buccino, A., et al. 2017, *A&A*, 600, A83, doi: [10.1051/0004-6361/201629152](https://doi.org/10.1051/0004-6361/201629152)
- Morin, J., Donati, J. F., Petit, P., et al. 2008, *MNRAS*, 390, 567, doi: [10.1111/j.1365-2966.2008.13809.x](https://doi.org/10.1111/j.1365-2966.2008.13809.x)
- Namekata, K., Sakaue, T., Watanabe, K., et al. 2017, *ApJ*, 851, 91, doi: [10.3847/1538-4357/aa9b34](https://doi.org/10.3847/1538-4357/aa9b34)
- Namekata, K., Maehara, H., Notsu, Y., et al. 2019, *ApJ*, 871, 187, doi: [10.3847/1538-4357/aaf471](https://doi.org/10.3847/1538-4357/aaf471)
- Namekata, K., Maehara, H., Honda, S., et al. 2021, *Nature Astronomy*, 6, 241, doi: [10.1038/s41550-021-01532-8](https://doi.org/10.1038/s41550-021-01532-8)
- Newton, E. R., Irwin, J., Charbonneau, D., et al. 2016, *ApJ*, 821, 93, doi: [10.3847/0004-637X/821/2/93](https://doi.org/10.3847/0004-637X/821/2/93)
- Notsu, Y., Shibayama, T., Maehara, H., et al. 2013, *ApJ*, 771, 127, doi: [10.1088/0004-637X/771/2/127](https://doi.org/10.1088/0004-637X/771/2/127)
- Notsu, Y., Maehara, H., Honda, S., et al. 2019, *ApJ*, 876, 58, doi: [10.3847/1538-4357/ab14e6](https://doi.org/10.3847/1538-4357/ab14e6)
- Paudel, R. R., Gizis, J. E., Mullan, D. J., et al. 2020, *MNRAS*, 494, 5751, doi: [10.1093/mnras/staa1137](https://doi.org/10.1093/mnras/staa1137)
- . 2018, *ApJ*, 861, 76, doi: [10.3847/1538-4357/aac8e0](https://doi.org/10.3847/1538-4357/aac8e0)
- Pettersen, B. R. 1989, *International Astronomical Union Colloquium*, 104, 299–312, doi: [10.1017/S025292110003195X](https://doi.org/10.1017/S025292110003195X)
- Pietras, M., Falewicz, R., Siarkowski, M., Bicz, K., & Preś, P. 2022, *ApJ*, 935, 143, doi: [10.3847/1538-4357/ac8352](https://doi.org/10.3847/1538-4357/ac8352)
- Pietras, M., Falewicz, R., Siarkowski, M., et al. 2023, *ApJ*, 954, 19, doi: [10.3847/1538-4357/ace69a](https://doi.org/10.3847/1538-4357/ace69a)
- Rebull, L. M., Stauffer, J. R., Bouvier, J., et al. 2016a, *AJ*, 152, 113, doi: [10.3847/0004-6256/152/5/113](https://doi.org/10.3847/0004-6256/152/5/113)

- . 2016b, *AJ*, 152, 114, doi: [10.3847/0004-6256/152/5/114](https://doi.org/10.3847/0004-6256/152/5/114)
- Reiners, A., & Basri, G. 2009, *A&A*, 496, 787, doi: [10.1051/0004-6361:200811450](https://doi.org/10.1051/0004-6361:200811450)
- Ricker, G. R., Winn, J. N., Vanderspek, R., et al. 2015, *Journal of Astronomical Telescopes, Instruments, and Systems*, 1, 014003, doi: [10.1117/1.JATIS.1.1.014003](https://doi.org/10.1117/1.JATIS.1.1.014003)
- Roettenbacher, R. M., & Vida, K. 2018, *ApJ*, 868, 3, doi: [10.3847/1538-4357/aae77e](https://doi.org/10.3847/1538-4357/aae77e)
- Savitzky, A., & Golay, M. J. E. 1964, *Analytical Chemistry*, 36, 1627, doi: [10.1021/ac60214a047](https://doi.org/10.1021/ac60214a047)
- Scargle, J. D. 1982, *ApJ*, 263, 835, doi: [10.1086/160554](https://doi.org/10.1086/160554)
- Shibata, K., & Yokoyama, T. 1999, *ApJL*, 526, L49, doi: [10.1086/312354](https://doi.org/10.1086/312354)
- Shibayama, T., Maehara, H., Notsu, S., et al. 2013, *ApJS*, 209, 5, doi: [10.1088/0067-0049/209/1/5](https://doi.org/10.1088/0067-0049/209/1/5)
- Slesnick, C. L., Carpenter, J. M., Hillenbrand, L. A., & Mamajek, E. E. 2006, *AJ*, 132, 2665, doi: [10.1086/508937](https://doi.org/10.1086/508937)
- Stassun, K. G., Oelkers, R. J., Paegert, M., et al. 2019, *AJ*, 158, 138, doi: [10.3847/1538-3881/ab3467](https://doi.org/10.3847/1538-3881/ab3467)
- Strassmeier, K. G. 2009, *A&A Rv*, 17, 251, doi: [10.1007/s00159-009-0020-6](https://doi.org/10.1007/s00159-009-0020-6)
- Torres, C. A. O., Quast, G. R., da Silva, L., et al. 2006, *A&A*, 460, 695, doi: [10.1051/0004-6361:20065602](https://doi.org/10.1051/0004-6361:20065602)
- Tu, Z.-L., Yang, M., Wang, H. F., & Wang, F. Y. 2021, *ApJS*, 253, 35, doi: [10.3847/1538-4365/abda3c](https://doi.org/10.3847/1538-4365/abda3c)
- Tu, Z.-L., Yang, M., Zhang, Z. J., & Wang, F. Y. 2020, *ApJ*, 890, 46, doi: [10.3847/1538-4357/ab6606](https://doi.org/10.3847/1538-4357/ab6606)
- Vach, S., Zhou, G., Huang, C. X., et al. 2024, *AJ*, 167, 210, doi: [10.3847/1538-3881/ad3108](https://doi.org/10.3847/1538-3881/ad3108)
- Valenti, J. A., Marcy, G. W., & Basri, G. 1995, *ApJ*, 439, 939, doi: [10.1086/175231](https://doi.org/10.1086/175231)
- Van Rossum, G., & Drake, F. L. 2009, *Python 3 Reference Manual* (Scotts Valley, CA: CreateSpace)
- Veronig, A. M., Rybák, J., Gömöry, P., et al. 2010, *ApJ*, 719, 655, doi: [10.1088/0004-637X/719/1/655](https://doi.org/10.1088/0004-637X/719/1/655)
- Vida, K., Oláh, K., Kővári, Z., et al. 2019, *ApJ*, 884, 160, doi: [10.3847/1538-4357/ab41f5](https://doi.org/10.3847/1538-4357/ab41f5)
- Vida, K., Kővári, Z., Leitzinger, M., et al. 2024, *Universe*, 10, 313, doi: [10.3390/universe10080313](https://doi.org/10.3390/universe10080313)
- Vidotto, A. A., Gregory, S. G., Jardine, M., et al. 2014, *MNRAS*, 441, 2361, doi: [10.1093/mnras/stu728](https://doi.org/10.1093/mnras/stu728)
- Wright, N. J., Drake, J. J., Mamajek, E. E., & Henry, G. W. 2011, *ApJ*, 743, 48, doi: [10.1088/0004-637X/743/1/48](https://doi.org/10.1088/0004-637X/743/1/48)
- Yang, H., & Liu, J. 2019, *ApJS*, 241, 29, doi: [10.3847/1538-4365/ab0d28](https://doi.org/10.3847/1538-4365/ab0d28)
- Yang, Z., Zhang, L., Meng, G., et al. 2023, *A&A*, 669, A15, doi: [10.1051/0004-6361/202142710](https://doi.org/10.1051/0004-6361/202142710)